Available online at www.sciencedirect.com
SCIENCE DIRECT®
Journal of Computational Physics 197 (2004) 418–459
JOURNAL OF COMPUTATIONAL PHYSICS
www.elsevier.com/locate/jcp

Space–time coupled spectral/*hp* least-squares finite element formulation for the incompressible Navier–Stokes equations

J.P. Pontaza *, J.N. Reddy

Department of Mechanical Engineering, Texas A&M University, College Station, TX 77843-3123, USA

Received 18 September 2002; received in revised form 29 October 2003; accepted 28 November 2003
Available online 22 January 2004

Abstract

We consider least-squares finite element models for the numerical solution of the non-stationary Navier–Stokes equations governing viscous incompressible fluid flows. The paper presents a formulation where the effects of space and time are coupled, resulting in a true space–time least-squares minimization procedure, as opposed to a space–time decoupled formulation where a least-squares minimization procedure is performed in space at each time step. The formulation is first presented for the linear advection-diffusion equation and then extended to the Navier–Stokes equations. The formulation has no time step stability restrictions and is spectrally accurate in both space and time. To allow the use of practical C^0 element expansions in the resulting finite element model, the Navier–Stokes equations are expressed as an equivalent set of first-order equations by introducing vorticity as an additional independent variable and the least-squares method is used to develop the finite element model of the governing equations. High-order element expansions are used to construct the discrete model. The discrete model thus obtained is linearized by Newton's method, resulting in a linear system of equations with a symmetric positive definite coefficient matrix that is solved in a fully coupled manner by a preconditioned conjugate gradient method in matrix-free form. Spectral convergence of the L_2 least-squares functional and L_2 error norms in space–time is verified using a smooth solution to the two-dimensional non-stationary incompressible Navier–Stokes equations. Numerical results are presented for impulsively started lid-driven cavity flow, oscillatory lid-driven cavity flow, transient flow over a backward-facing step, and flow around a circular cylinder; the results demonstrate the predictive capability and robustness of the proposed formulation. Even though the space–time coupled formulation is emphasized, we also present the formulation and numerical results for least-squares space–time decoupled finite element models. The numerical results show that the space–time coupled formulation has superior predictive capabilities for flows demanding high space–time resolution, exemplified here by the transient flow over a backward-facing step.

Keywords: Space–time coupled formulation; Spectral methods; *hp* methods; Least-squares; Incompressible flow

* Corresponding author. Tel.: +1-979-862-4037; fax: +1-979-845-3081.
E-mail addresses: pontaza@tamu.edu (J.P. Pontaza), jnreddy@shakti.tamu.edu (J.N. Reddy).
URL: http://people.tamu.edu/~pontaza/.

0021-9991/$ - see front matter © 2003 Elsevier Inc. All rights reserved.
doi:10.1016/j.jcp.2003.11.030

1. Introduction

In previous work [1], we presented a least-squares finite element formulation for the stationary Navier–Stokes equations where the discrete model was developed using high-order element nodal/modal expansions; here we extend the formulation to the non-stationary case using a space–time coupled least-squares formulation.

Traditionally, the weak form Galerkin finite element formulation of time-dependent problems involves two steps [2,3]: *Spatial approximation,* where we assume that the solution is separable into functions of space only and time only; the spatial finite element model is developed using the procedures of static problems, while carrying all time dependent terms in the formulation. This step results in a semidiscrete system of ordinary differential equations in time for the element degrees of freedom. *Temporal approximation,* where the semidiscrete model is further approximated in time, using finite difference formulae for the time derivatives. This two-step procedure provides a good approximation to the time-dependent evolution of the problem, provided the time step is small enough to meet stability and accuracy criteria.

The traditional least-squares finite element formulation of time-dependent problems also involves two steps [4,5]: *Temporal approximation,* where the temporal operator is directly approximated and replaced by finite difference formulae. In contrast with the weak form Galerkin formulation of time-dependent problems, the temporal approximation is performed first and yields a modified governing equation or sets of governing equations if a multi-stage temporal approximation is used. *Spatial approximation,* where the (spatial) least-squares functional, defined as the sum of the squares of the modified governing equation(s) residuals measured in suitable norms of Hilbert spaces, is minimized. In the time-marching procedure, the space integral is minimized at each time step. Both formulations described above are space–time decoupled formulations.

Least-squares finite element formulations offer several theoretical and computational advantages over the weak form Galerkin formulation for the incompressible Navier–Stokes equations (see, e.g., [6,7]). In particular, circumventing the inf–sup condition, thus allowing approximation spaces for velocities and pressure to be chosen independently, including the choice of equal-order interpolation. Furthermore, the resulting algebraic problem will have a symmetric positive definite (SPD) coefficient matrix, which can be solved by using robust and fast iterative methods, such as preconditioned conjugate gradient (PCG) methods.

However, unlike the weak form Galerkin formulation where regularity requirements of the finite element spaces are weakened by the integration by parts step, least-squares based formulations have associated with them the requirement of higher regularity of the finite element spaces – dictated by the differentiability requirements of the governing equation(s) under consideration. To reduce the higher regularity requirements, the governing equation(s) are first transformed into an equivalent lower order system by introducing additional independent variables and then formulating the least-squares model based on the equivalent lower order system. Thus, to allow the use of practical C^0 nodal/modal expansions in the resulting finite element model, the Navier–Stokes equations are first recast as an equivalent first-order system and the least-squares functional defined in terms of L_2 norms only [1,4,6–9].

First-order systems that allow the construction of a L_2 least-squares functional that is H^1-norm equivalent are commonly referred to as H^1-coercive formulations. Such systems yield optimal error estimates with respect to the H^1-norm for all variables [7] and ensure the optimality of multiplicative and additive multigrid methods [8], which could be used either as a solver or a preconditioner for the conjugate gradient method. However, not all L_2 least-squares formulations are H^1-coercive. Such formulations are termed *non-equivalent* formulations, because the L_2 least-squares functional does not define an equivalent norm in H^1. Nevertheless, a *non-equivalent* formulation does not imply that the method is not optimal. It simply means that the optimality of the resulting method cannot be established a priori using standard elliptic theory.

In the context of least-squares finite element formulations for the Navier–Stokes equations, predominantly low order nodal expansions have been used to develop the discrete finite element model (see [4] and references therein). When the L_2 least-squares functional is not H^1-norm equivalent (defining a *non-equivalent* formulation), low order nodal expansions tend to lock and non-standard least-squares procedures such as collocation must be used to obtain acceptable numerical results. This is the preferred procedure in the work presented by Jiang [4] and Tang et al. [5], although they refer to the collocation solution as a reduced integration solution. It is important to note that reduced integration techniques will only result in a collocation solution if a strict balance between the number of collocation points and total number of degrees of freedom is satisfied. Thus, in general, blind application of reduced integration techniques will not result in a collocation solution. In addition, the least-squares functional cannot be used to measure the quality of the solution as it identically vanishes at the collocation points.

Even though a *non-equivalent* formulation departs from the ideal mathematical setting, it does not lead to disastrous results; as a violation of the inf–sup condition would, in a mixed weak form Galerkin formulation. As shown in our previous work [1] and in the work of Proot et al. [9], when high-order element nodal/modal expansions are used to construct the discrete finite element model, *non-equivalent* formulations are able to recover optimal properties. For smooth solutions, the L_2 least-squares functional decays exponentially fast as the element expansion order (p-level) is increased.

We realize that a least-squares space–time decoupled formulation is not desirable as it does not lend itself naturally to p-type refinement in time. Furthermore, a space–time decoupled formulation only applies least-squares variational principles in space and therefore cannot represent a true error minimization procedure of the time-dependent problem which describes an evolution in space–time domain. This provided the motivation to develop a space–time coupled least-squares formulation, which represents a true minimization procedure in space–time domain.

Invariably, we as analysts would like to simulate and study the time evolution of an initial value problem for large values of time. This would require a space–time mesh with a large number of elements in time. The size of the resulting set of assembled algebraic equations could be large and prohibitively expensive in terms of available computer memory and non-optimal in terms of CPU solve time. To alleviate the drawbacks, we adopt a time-stepping procedure in which the solution is obtained for space–time strips in a sequential manner. The initial conditions for the current space–time strip are obtained from the latest space plane from the previous space–time strip. Hence, for each space–time strip we solve a true initial boundary value problem.

Having introduced a basis in the time domain allows us to represent the time evolution with arbitrary accuracy, which eliminates the question of stability of the time-stepping procedure. This means that we can choose the length (Δt) of the space–time strip as large as we wish, the only issue is accuracy; which we can control by hp refinements in time.

Note that a two-dimensional time-dependent problem needs a three-dimensional space–time mesh. Even after adopting the time-stepping procedure, storage of the assembled stiffness matrix in banded or in compressed sparse row/column format is prohibitively expensive in terms of computer memory. We therefore resort to matrix-free techniques, also known as element-by-element solution algorithms.

Bell and Surana [10,11] presented numerical results for the non-stationary incompressible Navier–Stokes equations. They used the stress based first-order system and a space–time coupled least-squares formulation with a modal basis derived from equispaced Lagrange polynomials. They presented time history results for impulsively started Couette flow and the lid-driven cavity flow problem. In the present study we consider the numerical solution of the non-stationary incompressible Navier–Stokes equations using a vorticity based first-order system. We make use of the nodal and modal expansions for quadrilateral elements due to Warburton et al. [12,13]. We present time history results for flows which have a true steady-state solution and a periodic steady-state solution.

The paper is organized as follows. As a preliminary step to the Navier–Stokes equations, in Section 2, we present the space–time coupled least-squares formulation for the non-stationary advection-diffusion equation. We give details on the finite element model and the nodal/modal expansions used throughout the paper, followed by a discussion regarding the accuracy, stability, and computational cost of space–time coupled and decoupled formulations. Numerical results for the pure advection of a cosine hill in a rotating flow field are presented to conclude this section. In Section 3 we present the space–time coupled least-squares formulation for the non-stationary incompressible Navier–Stokes equations. The Navier–Stokes equations are expressed as an equivalent set of first-order equations by introducing vorticity as an additional independent variable and the least-squares method is used to develop the finite element model. Numerical results using the proposed formulation are presented in Section 4. Exponentially fast decay (spectral convergence) of the L_2 least-squares functional and L_2 error norms in space–time is verified using a smooth solution to the two-dimensional non-stationary incompressible Navier–Stokes equations. We present numerical results for impulsively started lid-driven cavity flow, oscillatory lid-driven cavity flow, transient flow over a backward-facing step, and flow past a circular cylinder. Cost metrics are presented for each of the benchmark problems to show the performance of the iterative solver. Comparisons between space–time coupled and decoupled formulations, in terms of predictive capabilities and cost, are presented for the benchmarks problems of transient flow over a backward-facing step and flow past a circular cylinder. In Section 5 we give concluding remarks.

2. The advection-diffusion equation

Let $\bar{\Omega}$ be the closure of an open bounded region Ω in $\mathbb{R}^n$, where $n = 2$ or 3 represents the number of space dimensions, and $\mathbf{x} = (x_1, \ldots, x_n) = (x, y, z)$ be a point in $\bar{\Omega} = \Omega \cup \partial\Omega$, where $\partial\Omega = \Gamma$ is the boundary of Ω. We consider the solution of the non-stationary linear advection-diffusion equation in dimensionless form, which can be stated as follows:

Find $\phi(\mathbf{x}, t)$ such that

$$\frac{\partial \phi}{\partial t} + (\mathbf{u} \cdot \nabla)\phi - \frac{1}{Pe}\nabla^2 \phi = f \quad \text{in } \Omega \times (0, \tau], \tag{1}$$

$$\phi(\mathbf{x}, 0) = {}^0\phi(\mathbf{x}) \quad \text{in } \Omega, \tag{2}$$

$$\phi = \phi^s \quad \text{on } \Gamma_\phi \times (0, \tau], \tag{3}$$

$$\hat{\mathbf{n}} \cdot \nabla \phi = q_n^s \quad \text{on } \Gamma_q \times (0, \tau], \tag{4}$$

where $\Gamma = \Gamma_\phi \cup \Gamma_q$ and $\Gamma_\phi \cap \Gamma_q = \emptyset$, τ is a real number (time) > 0, Pe is the Peclet number, $\mathbf{u}$ is the prescribed velocity field, f is the source term, $\hat{\mathbf{n}}$ is the outward unit normal on the boundary of Ω, ϕ^s is the prescribed value of ϕ on the boundary Γ_ϕ, q_n^s is the prescribed normal flux on the boundary Γ_q, and in Eq. (2) the initial conditions are given.

Although direct application of least-squares variational principles to the advection-diffusion equation is possible it will result in an impractical least-squares finite element model as we would be required to work with continuously differentiable (C^1-continuous) finite element spaces. We proceed instead by first replacing the advection-diffusion problem, Eqs. (1)–(4) with its first-order system equivalent.

Find $\phi(\mathbf{x},t)$ and $\mathbf{q}(\mathbf{x},t)$ such that

$$\frac{\partial\phi}{\partial t}+(\mathbf{u}\cdot\nabla)\phi-\frac{1}{Pe}\nabla\cdot\mathbf{q}=f \quad \text{in } \Omega\times(0,\tau], \tag{5}$$

$$\nabla\phi-\mathbf{q}=\mathbf{0} \quad \text{in } \Omega\times(0,\tau], \tag{6}$$

$$\nabla\times\mathbf{q}=\mathbf{0} \quad \text{in } \Omega\times(0,\tau], \tag{7}$$

$$\phi(\mathbf{x},0)={}^0\phi(\mathbf{x}) \quad \text{in } \Omega, \tag{8}$$

$$\phi=\phi^s \quad \text{on } \Gamma_\phi\times(0,\tau], \tag{9}$$

$$\hat{\mathbf{n}}\cdot\mathbf{q}=q_n^s \quad \text{on } \Gamma_q\times(0,\tau], \tag{10}$$

where $\mathbf{q}$ is a vector valued function whose components are the fluxes of ϕ, defined in Eq. (6), and Eq. (7) is a curl constraint to ensure H^1 coercivity of the system [7].

A least-squares finite element model, where the least-squares functional is defined in terms of L_2 norms only, and is based on the equivalent first-order system, Eqs. (5)–(7), allows the use of practical C^0-continuous element expansions. The reduction in regularity requirements of the element expansions across inter-element boundaries came at the price of introducing additional independent variables, sometimes termed *auxiliary variables*. The additional variables imply an increase in cost, but can be argued to be beneficial as they may represent physically meaningful variables, fluxes in this case.

2.1. L_2 least-squares formulation

For $s\geqslant 0$, we use the standard notation and definition for the Sobolev spaces $H^s(\Omega)$ and $H^s(\Gamma)$ with corresponding inner products denoted by $(\cdot,\cdot)_{s,\Omega}$ and $(\cdot,\cdot)_{s,\Gamma}$ and norms by $\|\cdot\|_{s,\Omega}$ and $\|\cdot\|_{s,\Gamma}$, respectively. Whenever there is no chance of ambiguity, the measures Ω and Γ will be omitted from inner product and norm designations. We denote the $L_2(\Omega)$ and $L_2(\Gamma)$ inner products by $(\cdot,\cdot)$ and $(\cdot,\cdot)_\Gamma$, respectively. By $\mathbf{H}^s(\Omega)$ we denote the product space $[H^s(\Omega)]^n$. We denote by $H_0^1(\Omega)$ the space consisting of $H^1(\Omega)$ functions that vanish on the boundary Γ and by $\bar{L}_2(\Omega)$ the space of all square integrable functions with zero mean with respect to Ω.

The L_2 least-squares functional associated with the equivalent first order system of the advection-diffusion problem is

$$\mathscr{J}(\phi,\mathbf{q};f)=\frac{1}{2}\left(\left\|\frac{\partial\phi}{\partial t}+(\mathbf{u}\cdot\nabla)\phi-\frac{1}{Pe}\nabla\cdot\mathbf{q}-f\right\|^2_{0,\Omega\times(0,\tau]}+\|\nabla\phi-\mathbf{q}\|^2_{0,\Omega\times(0,\tau]}+\|\nabla\times\mathbf{q}\|^2_{0,\Omega\times(0,\tau]}\right), \tag{11}$$

where $\|\cdot\|_{0,\Omega\times(0,\tau]}$ denotes the L_2 norm of the enclosed quantity in space–time, i.e.,

$$\|u\|^2_{0,\Omega\times(0,\tau]}=\int_0^\tau\int_\Omega |u|^2\,\mathrm{d}\Omega\,\mathrm{d}t. \tag{12}$$

Considering homogeneous boundary data and denoting the space–time domain by $\Lambda=\bar{\Omega}\times(0,\tau]$, the least-squares principle for functional (11) can be stated as

Find $(\phi,\mathbf{q})\in\mathbf{X}$, $\phi(\mathbf{x},0)={}^0\phi(\mathbf{x})$ such that for all $(\psi,\mathbf{r})\in\mathbf{X}$

$$\mathscr{J}(\phi,\mathbf{q};f)\leqslant\mathscr{J}(\psi,\mathbf{r};f), \tag{13}$$

where we use the space

$$\mathbf{X} = \left\{ (\phi, \mathbf{q}) \in H^1(\Lambda) \times \mathbf{H}^1(\Lambda) \middle| \phi|_{\Gamma_\phi} = 0, \hat{\mathbf{n}} \cdot \mathbf{q}|_{\Gamma_q} = 0 \right\}.$$

It is easy to see that the Euler–Lagrange equation for this minimization problem is given by the following variational problem [14]:

Find $(\phi, \mathbf{q}) \in \mathbf{X}$, $\phi(\mathbf{x}, 0) = {}^0\phi(\mathbf{x})$ such that for all $(\psi, \mathbf{r}) \in \mathbf{X}$

$$\mathscr{B}((\phi, \mathbf{q}), (\psi, \mathbf{r})) = \mathscr{F}((\psi, \mathbf{r})), \tag{14}$$

where $\mathscr{B}$ is the symmetric form,

$$\mathscr{B}((\phi, \mathbf{u}), (\psi, \mathbf{r})) = \int_0^\tau \int_\Omega \left(\frac{\partial \phi}{\partial t} + (\mathbf{u} \cdot \nabla)\phi - \frac{1}{Pe} \nabla \cdot \mathbf{q} \right) \left(\frac{\partial \psi}{\partial t} + (\mathbf{u} \cdot \nabla)\psi - \frac{1}{Pe} \nabla \cdot \mathbf{r} \right) \mathrm{d}\Omega \, \mathrm{d}t + \int_0^\tau \int_\Omega (\nabla \phi - \mathbf{q}) \cdot (\nabla \psi - \mathbf{r}) \mathrm{d}\Omega \, \mathrm{d}t + \int_0^\tau \int_\Omega (\nabla \times \mathbf{q}) \cdot (\nabla \times \mathbf{r}) \mathrm{d}\Omega \, \mathrm{d}t$$

and $\mathscr{F}$ the functional,

$$\mathscr{F}((\psi, \mathbf{r})) = \int_0^\tau \int_\Omega f \left(\frac{\partial \psi}{\partial t} + (\mathbf{u} \cdot \nabla)\psi - \frac{1}{Pe} \nabla \cdot \mathbf{r} \right) \mathrm{d}\Omega \, \mathrm{d}t.$$

2.2. Finite element model

The finite element model is obtained by either restricting (14) to the finite dimensional subspace $\mathbf{X}_{hp}$ of the infinite dimensional space $\mathbf{X}$, or equivalently by minimizing (11) with respect to the chosen approximating spaces. Then the space–time coupled least-squares discrete finite element model for the advection-diffusion equation is given by the following discrete variational problem:

Find $(\phi^{hp}, \mathbf{q}^{hp}) \in \mathbf{X}_{hp}$, $\phi^{hp}(\mathbf{x}, 0) = {}^0\phi(\mathbf{x})$ such that for all $(\psi^{hp}, \mathbf{r}^{hp}) \in \mathbf{X}_{hp}$

$$\mathscr{B}\left(\left(\phi^{hp}, \mathbf{q}^{hp} \right), \left(\psi^{hp}, \mathbf{q}^{hp} \right) \right) = \mathscr{F}\left(\left(\psi^{hp}, \mathbf{r}^{hp} \right) \right). \tag{15}$$

We proceed to define a discrete problem by choosing appropriate finite element subspaces for ϕ and each of the components of the vector valued function $\mathbf{q} = (q_x, q_y, q_z)$. There are no restrictive compatibility conditions on the discrete spaces, so we choose the same finite element subspace for each of the primary variables. The only requirement on the approximating spaces is that we choose continuous piecewise polynomials that are at least bi-linear (in two dimensions) or tri-linear (in three dimensions).

We consider the two-dimensional case. As pointed out earlier, in a space–time coupled formulation, a time-dependent two-dimensional problem must be treated as a three-dimensional problem in space–time domain. Let the space–time domain $\bar{\Omega} \times (0, \tau]$ be denoted by $\bar{\Lambda}$ and let $\mathscr{P}_h = \{\mathscr{Q}\}$ be a family of brick finite elements $\bar{\Lambda}_e$ that make up the connected model $\bar{\Lambda}^h$ in space–time.

We map $\bar{\Lambda}_e$ to a bi-unit cube $\hat{\Lambda}_e = [-1, 1] \times [-1, 1] \times [-1, 1]$, where $\boldsymbol{\xi} = (\xi_1, \xi_2, \xi_3) = (\xi, \eta, \gamma)$ is a point in $\hat{\Lambda}_e$. Over a typical element $\hat{\Lambda}_e$ we approximate ϕ by the expression

$$\phi(\xi, \eta, \gamma) \approx \phi^{hp}(\xi, \eta, \gamma) = \sum_{j=1}^{n} \Delta_j \varphi_j(\xi, \eta, \gamma) \quad \text{in } \hat{\Lambda}_e. \tag{16}$$

In a modal expansion, φ_j are tensor products of the one-dimensional C^0 p-type hierarchical basis

$$\psi_i(\xi) = \begin{cases} \frac{1-\xi}{2} & i = 1, \\ \left(\frac{1-\xi}{2}\right)\left(\frac{1+\xi}{2}\right)P_{i-2}^{\alpha,\beta} & 2 \leqslant i \leqslant p,\ p \geqslant 2, \\ \frac{1+\xi}{2} & i = p+1, \end{cases} \tag{17}$$

and Δ_j are coefficients associated with each of the modes of the hierarchical basis. In definition (17) $P_p^{\alpha,\beta}$ are the Jacobi polynomials of order p. We use ultraspheric polynomials corresponding to the choice $\alpha = \beta$ with $\alpha = \beta = 0$ or 1.

In a nodal expansion, φ_j are tensor products of the one-dimensional C^0 spectral nodal basis

$$h_i(\xi) = \frac{(\xi-1)(\xi+1)L_p'(\xi)}{p(p+1)L_p(\xi_i)(\xi-\xi_i)} \tag{18}$$

and Δ_j are nodal values due to the Kronecker delta property of the spectral basis. In Eq. (18) $L_p = P_p^{0,0}$ is the Legendre polynomial of order p and ξ_i denotes the location of the roots of $(\xi-1)(\xi+1)L_p'(\xi) = 0$ in the interval $[-1,1]$. Details on the multidimensional construction of both the modal and nodal expansions can be found in [13].

We approximate the components of the vector valued function $\mathbf{q} = (q_x, q_y)$ in similar manner as we did for ϕ in Eq. (16) and proceed to generate a system of linear algebraic equations at the element level using Eq. (15). The integrals in Eq. (15) are evaluated using Gauss quadrature rules. In our implementation the Gauss–Legendre rules are used for both the modal and nodal expansions, and *full integration* is used to evaluate the integrals.

The global system of equations is assembled from the element contributions using the direct stiffness summation approach. The assembled system of equations can be written as

$$\begin{pmatrix} [K^{11}] & [K^{12}] & [K^{13}] \\ [K^{12}]^{\mathrm{T}} & [K^{22}] & [K^{23}] \\ [K^{13}]^{\mathrm{T}} & [K^{23}]^{\mathrm{T}} & [K^{33}] \end{pmatrix} \begin{pmatrix} \{\Delta^1\} \\ \{\Delta^2\} \\ \{\Delta^3\} \end{pmatrix} = \begin{pmatrix} \{F^1\} \\ \{F^2\} \\ \{F^3\} \end{pmatrix}, \tag{19}$$

where $\{\Delta^1\}, \{\Delta^2\}, \{\Delta^3\}$ are the modal/nodal unknown coefficients associated with ϕ, q_x, and q_y. For details on standard finite element methods, such as mapping $\bar{\Lambda}_e \rightleftarrows \hat{\Lambda}_e$, numerical integration in $\hat{\Lambda}_e$, and assembly using the direct stiffness summation approach see Reddy [2,3].

For large values of time, prohibitively large system of equations will be encountered. To reduce the computational cost we adopt a time-stepping procedure in which the solution is obtained for space–time strips in a sequential manner. At time t_{s+1} we solve the initial value problem in the space–time strip ${}_{s}^{s+1}\bar{\Lambda}^h = \bar{\Omega}^h \times (t_s, t_{s+1}]$ using as initial condition the solution from the space plane at time t_s from the space–time strip ${}_{s-1}^{s}\bar{\Lambda}^h = \bar{\Omega}^h \times (t_{s-1}, t_s]$. This procedure is continued until the desired time is reached.

2.3. Space–time decoupled and coupled formulations

2.3.1. Accuracy and stability

In space–time decoupled formulations, discretization in space and time are done independently. Traditionally, the temporal operators are represented by truncated Taylor series expansions in time domain. Such formulations result in an inherent approximation of the initial boundary value problem and thus the investigation of stability is essential. Representation of the temporal operator by high-order approximations, such as multi-step schemes, are only conditionally stable; imposing severe limitations on the size of the allowable time increment.

In the proposed formulation, the effects of space and time are allowed to remained coupled. There is no approximation of the initial boundary value problem. Instead, a basis is introduced in time domain to

represent the time evolution of the independent variables. Since the initial boundary value problem in each space–time strip is represented and solved with predetermined accuracy of order p, the question of stability does not arise. The only issue that remains is accuracy; which we can control by hp refinements in time. Furthermore, the L_2 least squares functional can provide an error measure for adaptive h, p, or hp refinements in space–time.

To further illustrate the differences between a space–time decoupled and coupled formulations, consider the following abstract initial boundary value problem:

$$\frac{\partial \mathbf{u}}{\partial t} + \mathscr{L}_{\mathbf{x}}(\mathbf{u}) = \mathbf{f} \quad \text{in } \Omega \times (0,\tau], \tag{20}$$

$$\mathscr{G}(\mathbf{u}) = \mathbf{h} \quad \text{on } \Gamma \times (0,\tau], \tag{21}$$

in which $\mathscr{L}_{\mathbf{x}}$ is a linear first-order partial differential operator in space acting on a vector $\mathbf{u}$ of unknowns, $\mathbf{f}$ is a known vector valued forcing function, $\mathscr{G}$ is a trace operator acting on $\mathbf{u}$, and $\mathbf{h}$ represents a known vector valued function on the boundary. We assume initial conditions are given and that the problem is well posed.

In a space–time decoupled formulation we first approximate the initial boundary value problem by replacing the temporal operator with a discrete equivalent. A popular choice are backward multi-step schemes, obeying the Dalquist stability barriers for an α-step stable scheme of order M_α. The modified problem is now:

$$\frac{\gamma_0}{\Delta t}\mathbf{u}^{s+1} - \sum_{q=0}^{M_\alpha - 1} \frac{\beta_q}{\Delta t}\mathbf{u}^{s-q} + \mathscr{L}_{\mathbf{x}}(\mathbf{u}^{s+1}) = \mathbf{f}^{s+1} \quad \text{in } \Omega, \tag{22}$$

$$\mathscr{G}(\mathbf{u}^{s+1}) = \mathbf{h}^{s+1} \quad \text{on } \Gamma, \tag{23}$$

where $\gamma_0 = \sum_{q=0}^{M_\alpha - 1} \beta_q$ for consistency, β_q are weights associated with a particular multi-step scheme, $\Delta t = t_{s+1} - t_s$ is the time increment, and it is implied that the modified problem will march in time. For sufficiently small Δt, the modified problem is equivalent to the original problem. To march the problem in time using a least-squares spatial finite element model, we must minimize the following space functional at each time step:

$$\mathscr{J}_{\Delta t}(\mathbf{u};\mathbf{f},\mathbf{h}) = \frac{1}{2}\left(\left\| \frac{\gamma_0}{\Delta t}\mathbf{u}^{s+1} - \sum_{q=0}^{M_\alpha - 1} \frac{\beta_q}{\Delta t}\mathbf{u}^{s-q} + \mathscr{L}_{\mathbf{x}}(\mathbf{u}^{s+1}) - \mathbf{f}^{s+1} \right\|^2_{0,\Omega} + \|\mathscr{G}(\mathbf{u}^{s+1}) - \mathbf{h}^{s+1}\|^2_{0,\Gamma} \right),$$

where the dependence on the time increment $\Delta t = t_{s+1} - t_s$ is evident. Once the discrete model is obtained, the eigen-spectrum of the amplification matrix needs to be examined and the time-step restriction determined as a function of an upper bound for the maximum eigenvalue; see [3]. The upper bound for the maximum eigenvalue will undoubtedly be highly dependent on the spatial expansion order, resulting in severe restrictions in the allowable time increment for high-order spatial expansions. Note that, unlike the weak form Galerkin formulation of time-dependent problems, a semidiscrete system of ordinary differential equations in time for the element degrees of freedom does not arise because the temporal approximation was performed first.

In a space–time coupled formulation we do not introduce any approximations to the initial boundary value problem, and minimize a functional in space–time domain:

$$\mathscr{J}(\mathbf{u};\mathbf{f},\mathbf{h}) = \frac{1}{2}\left(\left\| \frac{\partial \mathbf{u}}{\partial t} + \mathscr{L}_{\mathbf{x}}(\mathbf{u}) - \mathbf{f} \right\|^2_{0,\Omega\times[t_s,t_{s+1}]} + \|\mathscr{G}(\mathbf{u}) - \mathbf{h}\|^2_{0,\Gamma\times[t_s,t_{s+1}]} \right),$$

where the interval $[t_s, t_{s+1}]$ can be taken arbitrarily large, i.e., there are no restrictions on the size of the interval. In addition, this formulation naturally allows for p-type refinements in time.

2.3.2. Computational cost

Space–time decoupled formulations are commonly associated with reduced computational effort, when compared to space–time coupled formulations. Although this may hold true for low-order discrete models, it is not necessarily true for high-order models.

Simulations that literally require thousands of time steps in traditional space–time decoupled formulations can be accomplished in a few space–time strips using the proposed space–time coupled approach. As a result, the overall computational effort required by the space–time decoupled formulation may actually be greater than that for the space–time coupled formulation, rendering the coupled approach the most efficient for a spectral/*hp* least-squares formulation. Furthermore, the space–time coupled formulation will yield a *continuous* solution with predetermined accuracy of order p for all the independent variables in time domain. In contrast to a space–time decoupled formulation, where only point values of the independent variables are obtained in time domain.

The resulting algebraic problem will have a SPD coefficient matrix, which is solved in a fully coupled manner (i.e., no splitting) using a PCG method. PCG methods are considered to be the best option for an iterative solution of a linear system of equations with a SPD coefficient matrix. In the absence of round-off errors, the conjugate gradient method gives the exact solution of the linear system after at most N_{dof} (number of degrees of freedom) iteration steps [15]. In practice, the required number of iterations will be much smaller than N_{dof}.

The performance of an iterative method is invariably measured on how quickly the iterates converge to within an acceptable tolerance. The convergence rate of PCG methods is strongly dependent on the condition number of the (preconditioned) coefficient matrix [15,16]. A suitable preconditioner will effectively lower the condition number of the coefficient matrix and result in fast convergence of the iterates. Ideally, the preconditioner would be a cheap, good approximation to the exact Cholesky factor of the coefficient matrix.

For large N_{dof}, storage or sparse storage of the coefficient matrix is inconvenient and computer memory intensive. We therefore resort to storage-free techniques, also known as element-by-element solution algorithms, and implement a matrix-free version of the conjugate gradient method. The major disadvantage of the element-by-element data structure is the limited number of preconditioners that can be formulated from the unassembled matrices. In this work we choose a simple diagonal preconditioner, known as the Jacobi preconditioner [15], which does not require the assembly of the global coefficient matrix, not even an element matrix, which leads to tremendous savings in computer memory. In addition, the element-by-element nature of the algorithm naturally allows for its parallelization, resulting in considerable solve time speed-ups. Details of the PCG algorithms and construction of the Jacobi preconditioner can be found in [16,15] among many others.

2.4. Numerical example: advection of a cosine hill

We consider the two-dimensional transport of ϕ in a rotating flow field. The problem is defined in the finite region $\bar{\Omega} = [-2, 2] \times [-2, 2]$. The initial distribution of ϕ is prescribed to be in the form of a steep cosine hill with unit height. We are interested in pure advection of the initial distribution and to this end prescribe a high value for the Peclet number. The exact solution consists of a rigid rotation of the hill about $(x, y) = (0, 0)$. Undesirable features of the numerical solution are phase and dissipation errors.

The connected model in space–time, ${}_s{}^{s+1}\bar{\Lambda}^h = \bar{\Omega}^h \times [t_s, t_{s+1}]$ is shown in Fig. 1. It consists of a 6×6 uniform finite element mesh in space and a single element layer in time.

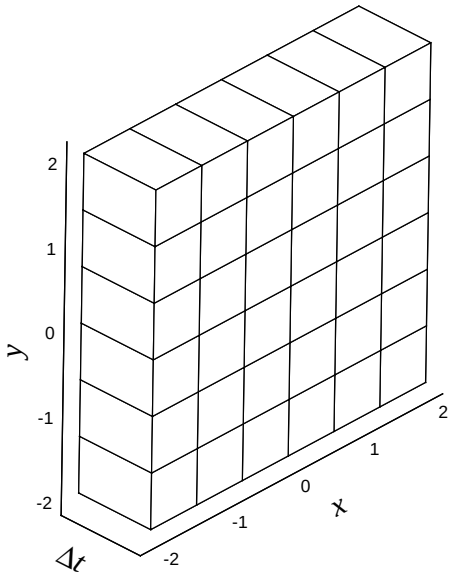

Fig. 1. Space–time computational domain and mesh for the advection of a cosine hill. The computational domain is a space–time strip, denoted by ${}_{s}^{s+1}\bar{\Lambda}^{h}$, with $\Delta t = t_{s+1} - t_s$.

The initial distribution is prescribed in the following form:

$$ {}^{0}\phi(x,y) = \begin{cases} \cos^2(\pi x)\cos^2(\pi y) & -1.5 \leqslant x \leqslant -0.5, -0.5 \leqslant y \leqslant 0.5, \\ 0 & \text{otherwise}, \end{cases} \tag{24} $$

together with homogeneous boundary conditions for ϕ. The velocity field is specified to be: $(u,v) = (-y,x)$. The initial conditions place the cosine hill at unit distance from $(x,y) = (0,0)$. Due to the nature of the prescribed velocity field all points in the flow field take a complete revolution in 2π units of time, i.e., a full rotation of the hill will take 2π units of time. The exact solution is thus identical at time t and $t + \mathscr{T}$, with $\mathscr{T} = 2\pi$.

The Peclet number considered here is 10^6. We use modal expansions with $p_\xi = p_\eta = 8$ and $p_\gamma = 4$ in each element, i.e. 8th order modal expansions in space and 4th order modal expansions in time, resulting in $N_{\text{dof}} = 36,015$ for a space–time strip. On each space–time strip the linear system of algebraic equations is solved using the matrix-free conjugate gradient algorithm with a Jacobi preconditioner. For the time marching procedure the size of the time step, $\Delta t = t_{s+1} - t_s$, was chosen as $\Delta t = 2\pi/20$; so that 20 time steps make one revolution. We march in time until $t = 50\mathscr{T}$, i.e., we let the cosine hill rotate 50 times around. Convergence of the conjugate gradient method was declared when the norm of the residual was less than 10^{-6}, which required 1729 ($0.048N_{\text{dof}}$) PCG iterations per space–time strip. The L_2 space–time least-squares functional remained below 10^{-5} throughout the time marching procedure.

We choose the points $(x,y) = (-1,0)$, $(0,-1)$, $(1,0)$, and $(0,1)$ to trace the time history of ϕ. The cosine hill should pass through these points in rigid body motion at a period of 2π. Fig. 2(a) shows the time history of ϕ through these points from $t = 0$ up to $t = 5\mathscr{T}$ and Fig. 2(b) from $t = 45\mathscr{T}$ up to $t = 50\mathscr{T}$. The results clearly show that the shape and height of the cosine hill did not change in time, meaning that numerical dissipation error is negligible. Furthermore, the cosine hill passes through the tracking points with a period of exactly 2π, meaning that phase error is negligible as well. The small oscillations near the steep base of the cosine hill are attributed to a lack of spatial resolution at this location.

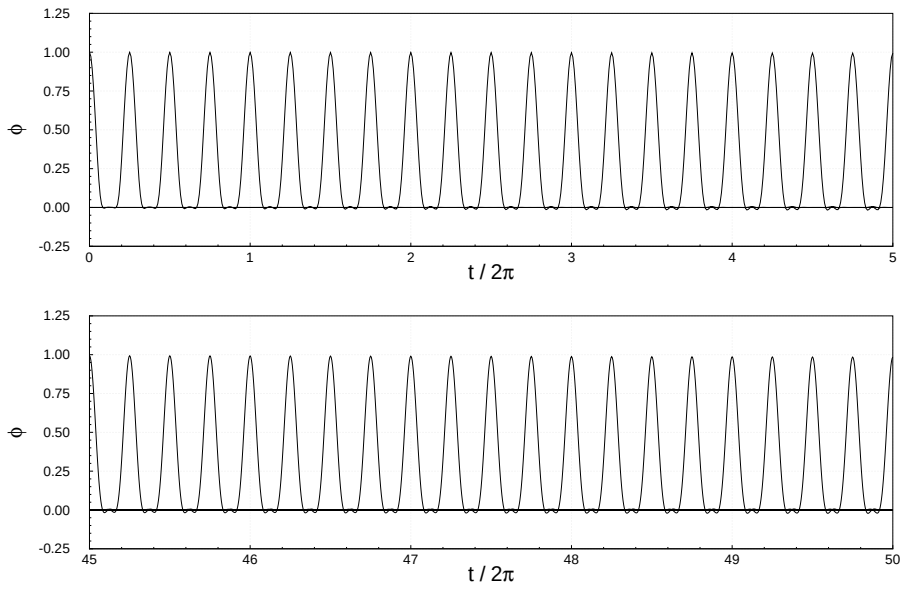

Fig. 2. Time history of ϕ at four selected locations: (a) from $t = 0$ up to $t = 5\mathscr{T}$ and (b) from $t = 45\mathscr{T}$ up to $t = 50\mathscr{T}$.

3. The incompressible Navier–Stokes equations

We consider the solution of the Navier–Stokes equations governing viscous incompressible fluid flows, which in dimensionless form can be stated as follows:

Find the velocity $\mathbf{u}(\mathbf{x}, t)$ and pressure $p(\mathbf{x}, t)$ such that

$$\frac{\partial \mathbf{u}}{\partial t} + (\mathbf{u} \cdot \nabla)\mathbf{u} + \nabla p - \frac{1}{Re}\nabla \cdot \left[(\nabla \mathbf{u}) + (\nabla \mathbf{u})^{\mathrm{T}}\right] = \mathbf{f} \quad \text{in } \Omega \times (0, \tau], \tag{25}$$

$$\nabla \cdot \mathbf{u} = 0 \quad \text{in } \Omega \times (0, \tau], \tag{26}$$

$$\mathbf{u}(\mathbf{x}, 0) = {}^{0}\mathbf{u}(\mathbf{x}) \quad \text{in } \Omega, \tag{27}$$

$$\mathbf{u} = \mathbf{u}^{s} \quad \text{on } \Gamma_u \times (0, \tau], \tag{28}$$

$$\hat{\mathbf{n}} \cdot \boldsymbol{\sigma} = \mathbf{f}^{s} \quad \text{on } \Gamma_f \times (0, \tau], \tag{29}$$

where $\Gamma = \Gamma_u \cup \Gamma_f$ and $\Gamma_u \cap \Gamma_f = \emptyset$, τ is a real number (time) > 0, $Re = \rho U_0 L/\mu$ is the Reynolds number, $\nabla \cdot {}^{0}\mathbf{u} = 0$, $\boldsymbol{\sigma} = -p\mathbf{I} + 1/\mathrm{Re}[(\nabla \mathbf{u}) + (\nabla \mathbf{u})^{\mathrm{T}}]$, $\mathbf{f}$ is a dimensionless force, $\hat{\mathbf{n}}$ is the outward unit normal on the boundary of Ω, $\mathbf{u}^{s}$ is the prescribed velocity on the boundary Γ_u, $\mathbf{f}^{s}$ are the prescribed tractions on the boundary Γ_f, and in Eq. (27) the initial conditions are given. We assume the problem is well posed.

In situations where outflow boundary conditions need to be modeled, the Navier–Stokes equations in the $\nabla^2\mathbf{u}$ form are preferred [17]. In such cases (using the incompressibility constraint given in Eq. (26)) we would drop the $(\nabla \mathbf{u})^{\mathrm{T}}$ term in Eq. (25), and the boundary conditions in Eq. (29) would then become

$$\hat{\mathbf{n}} \cdot \tilde{\boldsymbol{\sigma}} = \tilde{\mathbf{f}}^{s} \quad \text{on } \Gamma_f \times (0, \tau], \tag{30}$$

where $\tilde{\boldsymbol{\sigma}}$ is a pseudo-stress, $\tilde{\boldsymbol{\sigma}} = -p\mathbf{I} + (1/Re)\nabla \mathbf{u}$, and $\tilde{\mathbf{f}}^{s}$ are the prescribed pseudo-tractions on the boundary Γ_f, prescribed as zero at an outflow boundary.

To allow the use of practical C^0-continuous element expansions in the least-squares finite element model, the governing equations must be recast as an equivalent first-order system and the least-squares functional defined in terms of L_2 norms only. A least-squares finite element model can indeed be developed by using the Navier–Stokes equations in their strong form, however such formulation would require C^1 regularity of the finite element spaces across inter-element boundaries as a minimum requirement.

Here we consider a vorticity based first-order system. In two-dimensions the total number of variables is only increased by one and this formulation has the benefit of directly solving for a quantity of physical relevance, the vorticity.

3.1. The vorticity based first-order system

Introducing the vorticity vector, $\boldsymbol{\omega} = \nabla \times \mathbf{u}$, then by making use of the vector identity

$$\nabla \times \nabla \times \mathbf{u} = -\nabla^2 \mathbf{u} + \nabla(\nabla \cdot \mathbf{u})$$

and in view of the incompressibility constraint given in Eq. (26), the non-stationary Navier–Stokes equations, Eqs. (25)–(29), can be replaced by their first-order system equivalent:

Find the velocity $\mathbf{u}(\mathbf{x}, t)$, pressure $p(\mathbf{x}, t)$, and vorticity $\boldsymbol{\omega}(\mathbf{x}, t)$ such that

$$\frac{\partial \mathbf{u}}{\partial t} + (\mathbf{u} \cdot \nabla)\mathbf{u} + \nabla p + \frac{1}{Re} \nabla \times \boldsymbol{\omega} = \mathbf{f} \quad \text{in } \Omega \times (0, \tau], \tag{31}$$

$$\boldsymbol{\omega} - \nabla \times \mathbf{u} = \mathbf{0} \quad \text{in } \Omega \times (0, \tau], \tag{32}$$

$$\nabla \cdot \mathbf{u} = 0 \quad \text{in } \Omega \times (0, \tau], \tag{33}$$

$$\nabla \cdot \boldsymbol{\omega} = 0 \quad \text{in } \Omega \times (0, \tau], \tag{34}$$

$$\mathbf{u}(\mathbf{x}, 0) = {}^0\mathbf{u}(\mathbf{x}) \quad \text{in } \Omega, \tag{35}$$

$$\mathbf{u} = \mathbf{u}^s \quad \text{on } \Gamma_u \times (0, \tau], \tag{36}$$

$$\boldsymbol{\omega} = \boldsymbol{\omega}^s \quad \text{on } \Gamma_\omega \times (0, \tau]. \tag{37}$$

The seemingly redundant equation (34) is needed in the three dimensional case to make the system of equations uniformly elliptic [7]. Typically $\Gamma_u \cap \Gamma_\omega = \emptyset$, i.e., if velocity is specified at a boundary, vorticity need not be specified there. Outflow boundary conditions are imposed elegantly and efficiently in a weak sense through the least-squares functional [1].

3.1.1. L_2 least-squares formulation

The L_2 least-squares functional associated with the velocity–pressure–vorticity formulation is given by

$$\mathscr{J}(\mathbf{u}, p, \boldsymbol{\omega}; \mathbf{f}) = \frac{1}{2} \left(\left\| \frac{\partial \mathbf{u}}{\partial t} + (\mathbf{u} \cdot \nabla)\mathbf{u} + \nabla p + \frac{1}{Re} \nabla \times \boldsymbol{\omega} - \mathbf{f} \right\|^2_{0,\Omega \times (0,\tau]} + \|\boldsymbol{\omega} - \nabla \times \mathbf{u}\|^2_{0,\Omega \times (0,\tau]} + \|\nabla \cdot \mathbf{u}\|^2_{0,\Omega \times (0,\tau]} + \|\nabla \cdot \boldsymbol{\omega}\|^2_{0,\Omega \times (0,\tau]} \right). \tag{38}$$

Considering the homogeneous pure velocity boundary condition case, the least-squares principle for functional (38) can be stated as

Find $(\mathbf{u}, p, \boldsymbol{\omega}) \in \mathbf{X}$, $\mathbf{u}(\mathbf{x}, 0) = {}^0\mathbf{u}(\mathbf{x})$ such that for all $(\mathbf{v}, q, \boldsymbol{\psi}) \in \mathbf{X}$

$$\mathscr{J}(\mathbf{u}, p, \boldsymbol{\omega}; \mathbf{f}) \leqslant \mathscr{J}(\mathbf{v}, q, \boldsymbol{\psi}; \mathbf{f}), \tag{39}$$

where we use the space

$$\mathbf{X} = \left\{ (\mathbf{u}, p, \boldsymbol{\omega}) \in \mathbf{H}^1(\Lambda) \times H^1(\Lambda) \cap \bar{L}_2(\Lambda) \times \mathbf{H}^1(\Lambda) | \mathbf{u}|_{\Gamma_u} = \mathbf{0} \right\}.$$

Unlike the advection-diffusion equation, the Navier–Stokes equations are non-linear and suitable linearization procedures are required for its numerical solution. Such linearization procedures were not discussed in [1], and are detailed in the following. In general, there are two ways to approach the linearization procedure:

1. Linearize the governing equations first (using Picard or Newton linearization) – so that the least-squares functional is defined in terms of the linearized governing equations. Application of the least-squares method will yield a symmetric form. This approach is sometimes called "linearization by lagging coefficients", because the non-linearities are eliminated (or lagged) prior to the minimization step.
2. An alternate approach is to define the least-squares functional in terms of the non-linear equations. Application of the least-squares method will yield a non-symmetric form (due to the non-linearity). The resulting Euler–Lagrange equation is linearized using Newton's method at which point symmetry of the form is restored.

It is argued in [18] that the application of Newton's method to linearize the resulting Euler–Lagrange equation corresponding to the true least-squares functional defined using the non-linear governing equations (the second approach) is not the same as linearizing the governing equations by lagging coefficients and then constructing the least-squares functional and its minimization principle (the first approach). The underlying argument being that the construction of the least-squares functional together with its associated minimization principle and the method used to find the solution vector that satisfies theses conditions are two separate issues.

It is interesting to note, however, that when the governing equations are linearized by Newton's method prior to constructing the least-squares functional and its minimization principle, both approaches yield exactly the same (linearized) discrete finite element model. Here, the linearization procedure is illustrated using the second approach, for which the Euler–Lagrange equation is given by the following variational problem:

Find $(\mathbf{u}, p, \boldsymbol{\omega}) \in \mathbf{X}$, $\mathbf{u}(\mathbf{x}, 0) = {}^0\mathbf{u}(\mathbf{x})$ such that for all $(\mathbf{v}, q, \boldsymbol{\psi}) \in \mathbf{X}$

$$\mathscr{B}((\mathbf{u}, p, \boldsymbol{\omega}), (\mathbf{v}, q, \boldsymbol{\psi})) = \mathscr{F}((\mathbf{v}, q, \boldsymbol{\psi})), \tag{40}$$

where $\mathscr{B}$ is form,

$$\begin{aligned}\mathscr{B}((\mathbf{u}, p, \boldsymbol{\omega}), (\mathbf{v}, q, \boldsymbol{\psi})) = & \int_0^\tau \int_\Omega \left(\frac{\partial \mathbf{u}}{\partial t} + (\mathbf{u} \cdot \nabla)\mathbf{u} + \nabla p + \frac{1}{Re} \nabla \times \boldsymbol{\omega} \right) \cdot \left(\frac{\partial \mathbf{v}}{\partial t} + (\mathbf{v} \cdot \nabla)\mathbf{u} + (\mathbf{u} \cdot \nabla)\mathbf{v} \right. \\ & \left. + \nabla q + \frac{1}{Re} \nabla \times \boldsymbol{\psi} \right) \mathrm{d}\Omega \, \mathrm{d}t + \int_0^\tau \int_\Omega (\boldsymbol{\omega} - \nabla \times \mathbf{u}) \cdot (\boldsymbol{\psi} - \nabla \times \mathbf{v}) \mathrm{d}\Omega \, \mathrm{d}t \\ & + \int_0^\tau \int_\Omega (\nabla \cdot \mathbf{u})(\nabla \cdot \mathbf{v}) \mathrm{d}\Omega \, \mathrm{d}t + \int_0^\tau \int_\Omega (\nabla \cdot \boldsymbol{\omega})(\nabla \cdot \boldsymbol{\psi}) \mathrm{d}\Omega \, \mathrm{d}t\end{aligned}$$

and $\mathscr{F}$ the functional,

$$\mathscr{F}((\mathbf{v}, q, \boldsymbol{\psi})) = \int_0^\tau \int_\Omega \mathbf{f} \cdot \left(\frac{\partial \mathbf{v}}{\partial t} + (\mathbf{v} \cdot \nabla)\mathbf{u} + (\mathbf{u} \cdot \nabla)\mathbf{v} + \nabla q + \frac{1}{Re} \nabla \times \boldsymbol{\psi} \right) \mathrm{d}\Omega \, \mathrm{d}t.$$

At this point the form, $\mathscr{B}$, is non-symmetric and non-linear. Using Newton's method to linearize about a characteristic state $\mathbf{u}_0$, yields the *linearized* symmetric form,

$$\begin{aligned}\overline{\mathscr{B}}((\mathbf{u},p,\boldsymbol{\omega}),(\mathbf{v},q,\boldsymbol{\psi})) = &\int_0^\tau \int_\Omega \left(\frac{\partial \mathbf{u}}{\partial t} + (\mathbf{u}\cdot\nabla)\mathbf{u}_0 + (\mathbf{u}_0\cdot\nabla)\mathbf{u} + \nabla p + \frac{1}{Re}\nabla\times\boldsymbol{\omega}\right)\cdot\left(\frac{\partial \mathbf{v}}{\partial t} + (\mathbf{v}\cdot\nabla)\mathbf{u}_0\right.\\ &\left. + (\mathbf{u}_0\cdot\nabla)\mathbf{v} + \nabla q + \frac{1}{Re}\nabla\times\boldsymbol{\psi}\right)\mathrm{d}\Omega\,\mathrm{d}t + \int_0^\tau\int_\Omega (\boldsymbol{\omega}-\nabla\times\mathbf{u})\cdot(\boldsymbol{\psi}-\nabla\times\mathbf{v})\mathrm{d}\Omega\,\mathrm{d}t\\ &+ \int_0^\tau\int_\Omega (\nabla\cdot\mathbf{u})(\nabla\cdot\mathbf{v})\mathrm{d}\Omega\,\mathrm{d}t + \int_0^\tau\int_\Omega (\nabla\cdot\boldsymbol{\omega})(\nabla\cdot\boldsymbol{\psi})\mathrm{d}\Omega\,\mathrm{d}t\end{aligned}$$

and the functional,

$$\overline{\mathscr{F}}((\mathbf{v},q,\boldsymbol{\psi})) = \int_0^\tau\int_\Omega (\mathbf{f} + (\mathbf{u}_0\cdot\nabla)\mathbf{u}_0)\cdot\left(\frac{\partial \mathbf{v}}{\partial t} + (\mathbf{v}\cdot\nabla)\mathbf{u}_0 + (\mathbf{u}_0\cdot\nabla)\mathbf{v} + \nabla q + \frac{1}{Re}\nabla\times\boldsymbol{\psi}\right)\mathrm{d}\Omega\,\mathrm{d}t.$$

3.1.2. Finite element model

The finite element model is obtained by either restricting the linearized variational problem to the finite dimensional subspace $\mathbf{X}_{hp}$ of the infinite dimensional space $\mathbf{X}$, or equivalently by minimizing the linearized least-squares functional with respect to the chosen approximating spaces. Then the least-squares discrete finite element model for the incompressible Navier–Stokes equations is given by the following discrete variational problem:

Find $(\mathbf{u}^{hp},p^{hp},\boldsymbol{\omega}^{hp})\in\mathbf{X}_{hp}$, $\mathbf{u}^{hp}(\mathbf{x},0) = {}^0\mathbf{u}(\mathbf{x})$ such that for all $(\mathbf{v}^{hp},q^{hp},\boldsymbol{\psi}^{hp})\in\mathbf{X}_{hp}$

$$\overline{\mathscr{B}}\big((\mathbf{u}^{hp},p^{hp},\boldsymbol{\omega}^{hp}),(\mathbf{v}^{hp},q^{hp},\boldsymbol{\psi}^{hp})\big) = \overline{\mathscr{F}}\big((\mathbf{v}^{hp},q^{hp},\boldsymbol{\psi}^{hp})\big). \tag{41}$$

We proceed to define a discrete problem by choosing appropriate finite element subspaces for the velocity, pressure, and vorticity. There are no restrictive compatibility conditions on the discrete spaces, so we choose the same finite element subspace for all primary variables. Following the procedure outlined for the advection-diffusion problem, we generate a system of equations for the modal/nodal unknown coefficients associated with velocity, pressure, and vorticity. The discrete problem is solved in an iterative manner with respect to the Newton linearization.

4. Numerical examples

In the following, we present numerical results obtained with the proposed formulation. We start by verifying spectral convergence of the numerical algorithm using a manufactured closed form solution to the non-stationary Navier–Stokes equations. We then consider two-dimensional unsteady lid-driven cavity flows: impulsively started lid-driven cavity flow and oscillatory lid-driven cavity flow. Next, we consider transient two-dimensional flow over a backward-facing step. This problem proves to be a valuable benchmark, as it is well suited to compare the space–time coupled and decoupled formulations in terms of predictive capabilities and computational cost. In the last example, we consider two-dimensional unsteady flow past a circular cylinder.

4.1. Convergence

To verify spectral convergence, we use the method of manufactured solutions. The basic idea behind manufactured solutions is to simply come up with an exact solution, preferably one that is infinitely differentiable (i.e., smooth), not trivially reproduced by the element approximation functions (i.e., no poly-

nomials), and will exercise all the terms in the governing equation (or at least the ones we are interested in exercising).

We consider two-dimensional, unsteady flow in the bi-unit square, $\bar{\Omega} = [-1,1] \times [-1,1]$. We prescribe the closed form analytic solution to the non-stationary, incompressible Navier–Stokes equations to be of the form,

$$\begin{aligned} u(x,y,t) &= a_u + b_u \cos(\omega_u x)\sin(\omega_u y)\cos(\omega_{u,\tau} t), \\ v(x,y,t) &= a_v + b_v \sin(\omega_v x)\cos(\omega_{v,\tau} t), \\ p(x,y,t) &= a_p + b_p \sin(\omega_p y)\cos(\omega_{p,\tau} t). \end{aligned} \tag{42}$$

The prescribed analytic solution does not satisfy conservation of momentum or conservation of mass, i.e., if the above velocity and pressure fields are substituted into Eq. (25) (with $\mathbf{f} = \mathbf{0}$) and Eq. (26) a residual term for each of the equations will result. For the conservation of momentum, Eq. (25), a residual $\mathscr{R}^{\text{mom}}$ will result. Likewise, for the conservation of mass given by Eq. (26), a residual $\mathscr{R}^{\text{con}}$ will result. These residuals are simply treated as source terms, belonging to their respective equations, that produce the desired (prescribed) solution. These source terms or residuals are commonly referred to as *the consistent forcing functions*.

The choice of constants in Eq. (42) are shown in Table 1. The connected model in space–time, ${}_{s}^{s+1}\bar{A}^h = \bar{\Omega}^h \times [t_s, t_{s+1}]$, consists of a 4×4 uniform finite element mesh in space and a single element layer in time. Having chosen the space–time discretization, we now systematically increase the p-levels of the element approximation functions (in space–time) and expect the error measures to decay exponentially fast as the p-level is increased. In a logarithmic-linear scale the expected rate of convergence would appear as a straight line.

A suitable error measure is, for example, the L_2 least-squares functional ($\mathscr{J}$). Convergence of this measure to zero implies that the L_2 norm of the residuals of the governing equations are going to zero. An equally important error measure is the L_2 norm of the difference between the numerical solution and the analytic solution. Convergence of this measure to zero implies that the numerical solution approaches the exact solution. As a reminder, we note that the L_2 norm is defined over space–time; see Eq. (12).

The non-stationary incompressible Navier–Stokes equations in the vorticity based first-order form are discretized using the space–time coupled least-squares finite element formulation with nodal expansions in space–time. We take $\Delta t = t_{s+1} - t_s = 0.50$ and compute the solution in a single space–time strip for increasing expansion orders, $p_\xi = p_\eta = p_\gamma = p$. The exact solution is used to compute the initial condition and Dirichlet boundary conditions for the velocity components. Pressure was prescribed only at a point, i.e., a space–time line. In Fig. 3 we plot the L_2 least-squares functional and L_2 error of the velocity, pressure, and vorticity fields in space–time as a function of the expansion order in a logarithmic-linear scale. Exponentially fast decay (spectral convergence) of the L_2 least-squares functional and L_2 error is observed in space–time. Note that only algebraic decay in time would be observed using a space–time decoupled formulation.

Implicitly, Fig. 3 also verifies the unconditional stability of the space–time coupled formulation. In a space–time decoupled formulation as the order of the time approximation is increased the stability region for the time approximation decreases and a smaller time increment must be used to remain stable. Here we have continuously increased the order of the time approximation and kept $\Delta t = t_{s+1} - t_s$ constant at 0.50.

Table 1
Numerical values of the constants used in the exact solution, Eq. (42), to verify spectral convergence

	u	v	p
a	1.0	0.0	0.0
b	0.4	0.5	0.5
ω	2π	2π	2π
ω_τ	2π	2π	2π

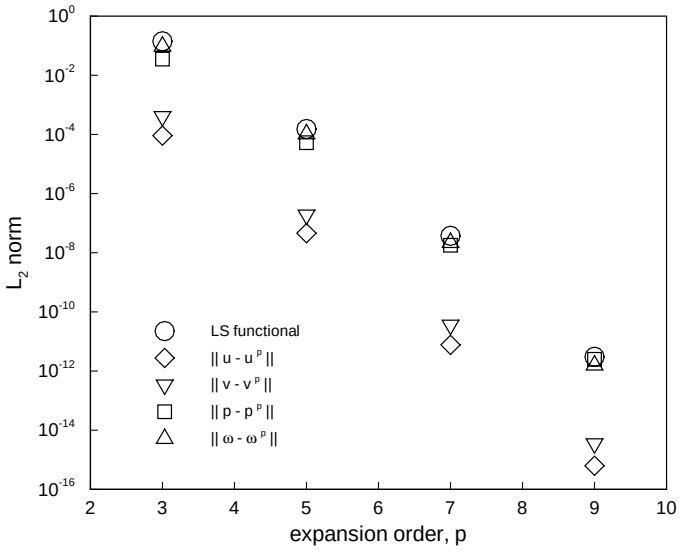

Fig. 3. Decay of the least-squares functional and convergence of the velocity, pressure, and vorticity space–time fields to the exact solution in the L_2 norm.

4.2. Impulsively started lid-driven cavity flow

We consider the two-dimensional flow of an incompressible fluid bounded in a square enclosure, $\bar{\Omega} = [0,1] \times [0,1]$. The fluid is initially at rest and is put into motion by the sudden translation of the top boundary. The connected model in space–time, ${}_{s}^{s+1}\bar{\Lambda}^h = \bar{\Omega}^h \times [t_s, t_{s+1}]$, is shown in Fig. 4. It consists of 6×6 finite elements in space and a single element layer in time.

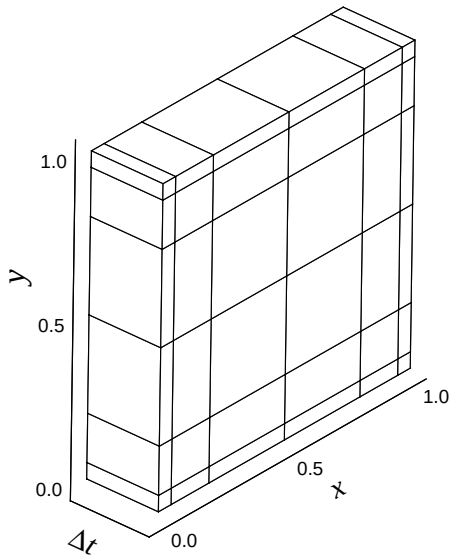

Fig. 4. Space–time computational domain and mesh for the lid-driven cavity problem. The computational domain is a space–time strip, denoted by ${}_{s}^{s+1}\bar{\Lambda}^h$, with $\Delta t = t_{s+1} - t_s$.

The boundary conditions are as follows: $u = v = 0$ on all solid walls, $p = 0$ at a point, and $u = u^s(x)$, $v = 0$ on the top driven surface ($y = 1.0$). On the driven surface we specify a hyperbolic tangent u-velocity distribution:

$$u_{\text{lid}}(x) = \begin{cases} \tanh(\beta x) & 0 \leqslant x \leqslant 0.5, \\ -\tanh(\beta(x-1)) & 0.5 < x \leqslant 1.0, \end{cases} \tag{43}$$

with $\beta > 0$. Here we take $\beta = 50$, which gives a smooth but at the same time sharp transition from $u = 0.0$ to $u = 1.0$ near the walls of the driven surface. This boundary condition results in a well-posed boundary condition, in the sense that singularities at the corners of the driven surface are eliminated. It closely emulates the standard (ill-posed) boundary condition where no transition is allowed between no-slip and the lid-driven velocity. The standard boundary condition (without additional h-refinement near the corners of the lid-driven surface) would destroy the high accuracy properties associated with the use of high-order expansions by polluting the solution near the corners (by inducing oscillatory behavior). High-order methods are sensitive to these types of singularities and in this sense are not as robust as low-order methods.

The u-velocity of the driven surface also varies in time according to a hyperbolic tangent distribution, $u_{\text{lid}}(t) = \tanh(t)$. This ensures a smooth and fast start-up translation of the driven surface. Both, spatial and temporal, distributions are shown in Fig. 5.

Note that the boundary conditions are imposed on space–time surfaces, so that the boundary condition $p = 0$ at a point translates into $p = 0$ in a space–time line. Similarly, $u = v = 0$ on all solid walls implies $u = v = 0$ on all space–time surfaces associated with a solid wall. On the space–time surface corresponding to the "driven surface", spatial and temporal variations need to be accounted for when specifying the boundary condition.

The Reynolds number considered here is 400. We use nodal expansions with $p_\xi = p_\eta = 5$ and $p_\gamma = 2$ in each element, resulting in $N_{\text{dof}} = 11,532$ for a space–time strip. At each Newton step the linear system of algebraic equations is solved using the matrix-free conjugate gradient algorithm with a Jacobi preconditioner.

For the time marching procedure the size of the time step, $\Delta t = t_{s+1} - t_s$, was chosen as $\Delta t = 0.2$ for $t \in (0, 2]$, $\Delta t = 0.5$ for $t \in (2, 10]$, and $\Delta t = 1.0$ for $t > 10$. We march in time until a steady-state is reached.

Convergence of the conjugate gradient method was declared when the norm of the residual was less than 10^{-6}. Nonlinear convergence was declared when the relative norm of the residual in velocities between two consecutive iterations was less than 10^{-4}, which typically required three Newton iterations per space–time

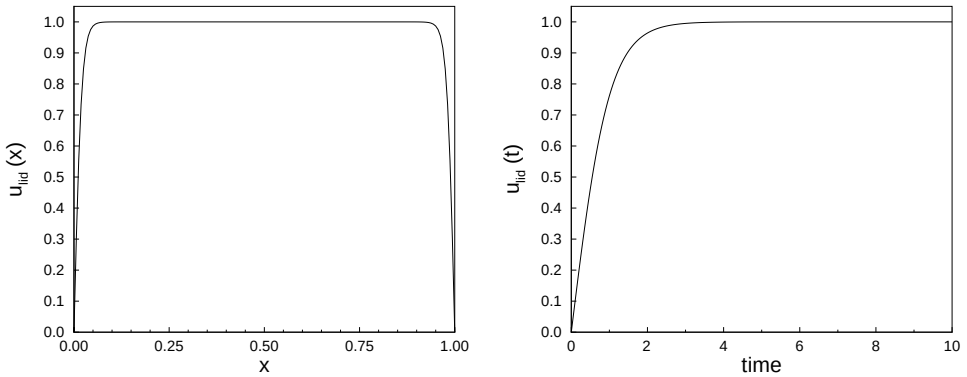

Fig. 5. Prescribed space–time u-velocity distributions on the driven surface of the cavity.

strip. Steady-state was declared when the relative norm of the residual in velocities between two consecutive space–time strips was less than 10^{-5}, which was reached at $t = 35$. The L_2 space–time least-squares functional remained below 10^{-3} throughout the time marching procedure.

Fig. 6 shows the time history of the flow by streamline plots. Upon start-up a long narrow vortex forms close to lid. The vortex gradually moves to the right and begins to grow. Around $t = 6$ the recirculation region in the lower right corner of the cavity appears. The primary vortex continues to broaden and moves towards its steady-state position.

Fig. 7 shows the time history of the u-velocity component at two locations along the vertical mid-line of the cavity, one 0.2 units away from the lid and the other 0.2 units away from the bottom surface. It is interesting to see that upon start-up the fluid close to the lid starts moving in the opposite direction. Fig. 8 shows the steady-state velocity profile along the vertical mid-line of the cavity. The steady-state solution is in excellent agreement with the benchmark solution of Ghia et al. [19].

In Fig. 9 we plot the time history of PCG iterations. The problem is non-linear, so each data point in the plot represents the sum of PCG iterations at each Newton step per space–time strip, thus representing the total number of PCG iterations per space–time strip. During the impulsive start of the lid, as much as 1300

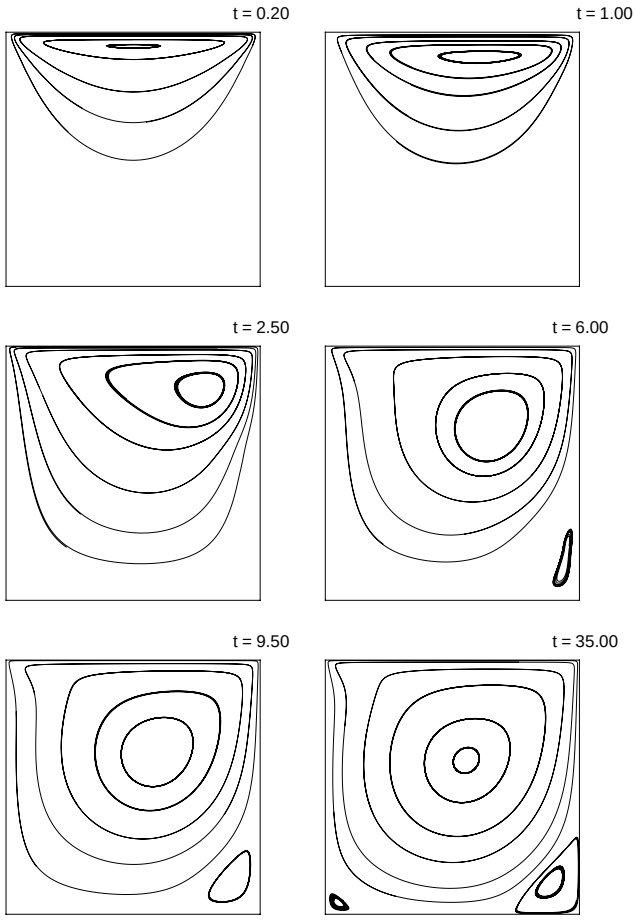

Fig. 6. Time history streamline plots for impulsively started lid-driven cavity flow at $Re = 400$.

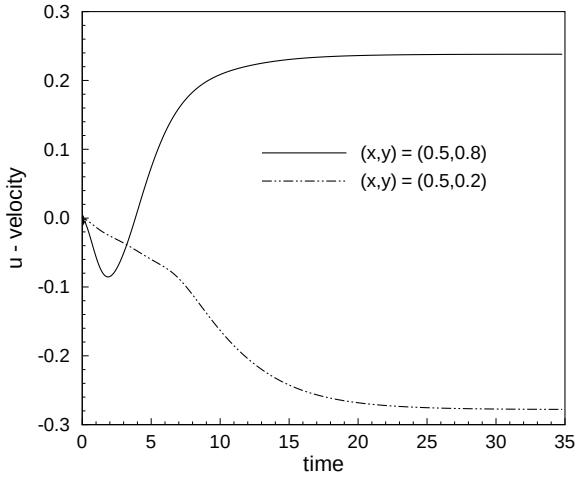

Fig. 7. Time history of the u-velocity component at two selected locations along the vertical mid-line of the cavity.

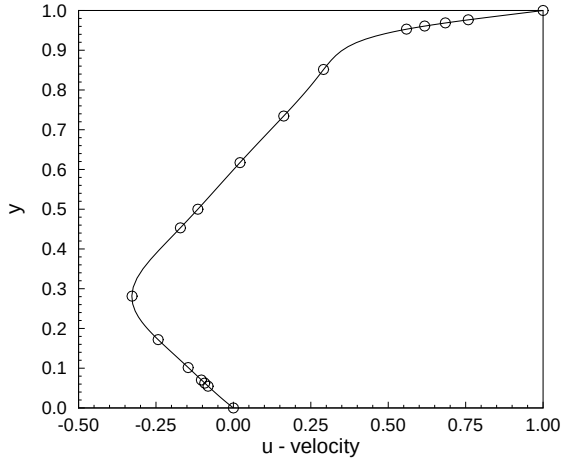

Fig. 8. Steady-state u-velocity profile along the vertical mid-line of the cavity for $Re = 400$: — computed, ○ Ghia et al. [19].

($0.113N_{\text{dof}}$) PCG iterations (using a Jacobi preconditioner) are required to meet non-linear and PCG convergence criteria. In the PCG iteration procedure, the solution from the previous space–time strip is used as an initial guess for the solution at the current strip, resulting in a reduction in the number of iterations required to achieve the PCG convergence tolerance as the numerical solution approaches the steady-state.

4.3. Oscillatory lid-driven cavity flow

Again, we consider the two-dimensional flow of an incompressible fluid bounded in a square enclosure, $\bar{\Omega} = [0,1] \times [0,1]$. The fluid is initially in a steady-state motion brought about by the translation of the top boundary. The top boundary suddenly begins to oscillate in a periodic fashion. The connected model in space–time is the same as that used for the impulsively started lid-driven cavity flow, and is shown in Fig. 4. It consists of 6×6 finite elements in space and a single element layer in time.

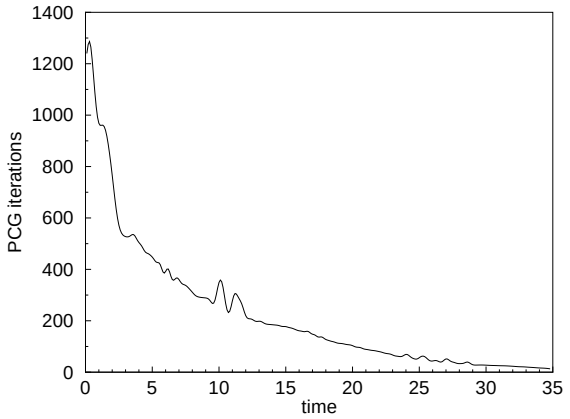

Fig. 9. Time history of PCG iterations for impulsively started lid-driven cavity flow ($Re = 400$). Jacobi preconditioner with stopping criteria $\varepsilon_{\mathrm{PCG}} = 10^{-6}$.

The boundary conditions are the same as that used for the impulsively started lid-driven cavity flow, with the exception that now the u-velocity of the driven surface varies in time according to the cosine distribution: $u_{\mathrm{lid}}(t) = \cos(t)$, with period $\mathscr{T} = 2\pi$.

The Reynolds number considered here is 400. We use nodal expansions with $p_\xi = p_\eta = 5$ and $p_\gamma = 2$ in each element, resulting in $N_{\mathrm{dof}} = 11,532$ for a space–time strip. At each Newton step the linear system of algebraic equations is solved using the matrix-free conjugate gradient algorithm with a Jacobi preconditioner. For the time marching procedure the size of the time step, $\Delta t = t_{s+1} - t_s$, was chosen as $\Delta t = 2\pi/20$; so that 20 time steps make one period. We march in time until a periodic steady-state is well established. Convergence of the conjugate gradient method was declared when the norm of the residual was less than 10^{-6}. Nonlinear convergence was declared when the relative norm of the residual in velocities between two consecutive iterations was less than 10^{-4}, which typically required three Newton iterations per space–time strip. The L_2 space–time least-squares functional remained below 10^{-3} throughout the time marching procedure.

Fig. 10 shows streamline plots at time $t = \mathscr{T}$, $2\mathscr{T}$, $4\mathscr{T}$, and $8\mathscr{T}$. It takes about six periods to reach the periodic steady-state at which the solution is identical at time t and $t + \mathscr{T}$. Fig. 11 shows the time history up to $t = 16\mathscr{T}$ of the u-velocity component at two locations along the vertical mid-line of the cavity, one 0.2 units away from the lid and the other 0.2 units away from the bottom surface. Streamline contour plots for the periodic steady-state solution are presented in Fig. 12 at the 8th cycle for $8\mathscr{T} \leqslant t \leqslant 9\mathscr{T}$. Fig. 12(a)–(h) correspond to the time sequence $t = 8\mathscr{T} + \beta\mathscr{T}$, where $\beta = 2/10$, 3/10, 4/10, 5/10, 7/10, 8/10, 9/10, 10/10. The property of mirror images is observed between Fig. 12(a)–(d) and (e)–(h) with respect to $x = 0.5$. Our results compare well with those by Iwatsu et al. [20] using the MAC method and Soh et al. [21] using an artificial compressibility method.

Fig. 13 shows the time history of PCG iterations for periodic steady-state flow conditions. Each data point in the plot represents the sum of PCG iterations at each Newton step per space–time strip, thus representing the total number of PCG iterations per space–time strip. In the PCG iteration procedure, the solution from the previous space–time strip is used as an initial guess for the solution at the current strip – explaining the sinuous behavior of the PCG iteration history. From Fig. 13 we see that, in the periodic steady-state, the total number of iterations required to meet non-linear and PCG convergence criteria per space–time strip varies between 1200 ($0.104N_{\mathrm{dof}}$) PCG iterations and 1600 ($0.139N_{\mathrm{dof}}$) PCG iterations (using a Jacobi preconditioner).

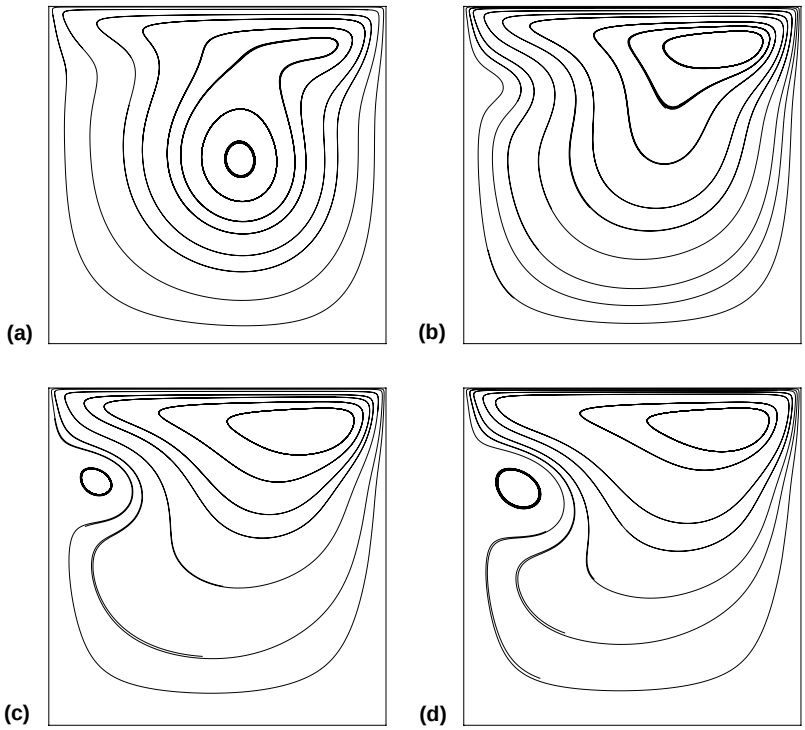

Fig. 10. Time history streamline plots for oscillatory lid-driven cavity flow for $Re = 400$: (a) $t = \mathscr{T}$, (b) $t = 2\mathscr{T}$, (c) $t = 4\mathscr{T}$, and (d) $t = 8\mathscr{T}$.

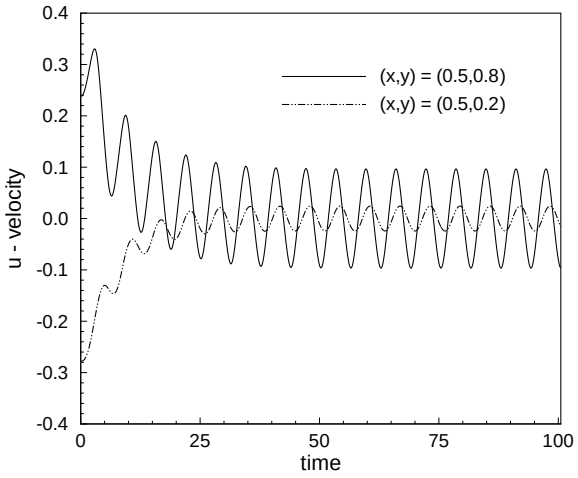

Fig. 11. Time history of the u-velocity component at two selected locations along the vertical mid-line of the cavity.

4.4. Transient flow over a backward-facing step

We consider the two-dimensional flow over a backward-facing step at $Re = 800$. In [1], we used the stationary form of the incompressible Navier–Stokes equations directly to develop the finite element model

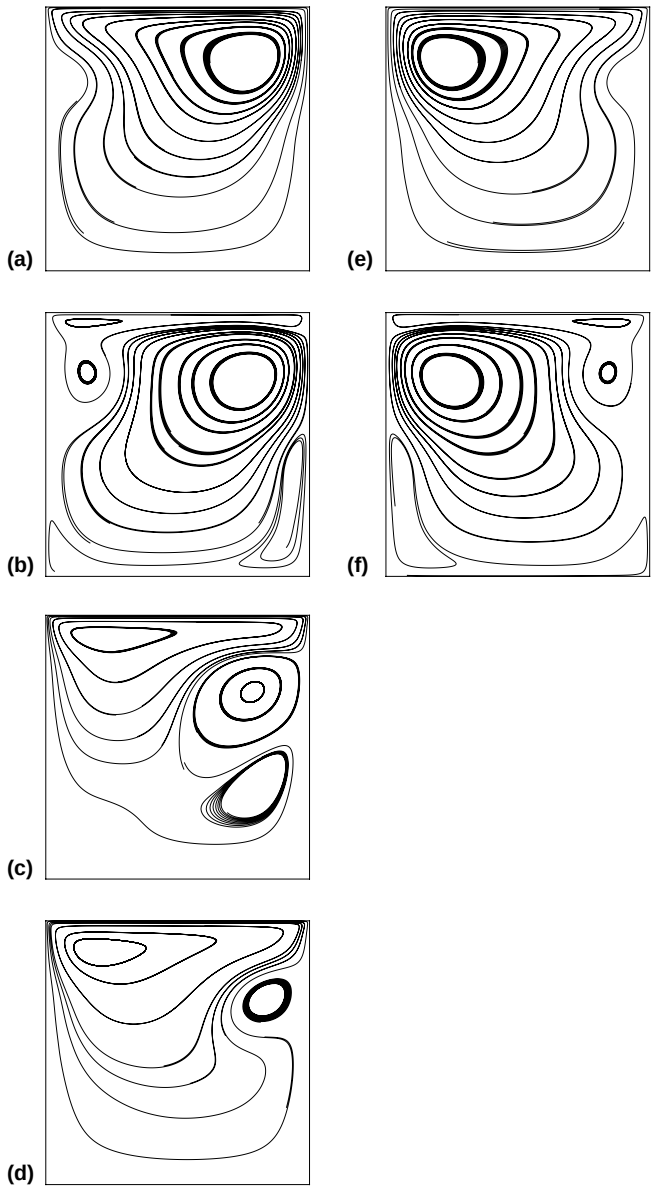

Fig. 12. Time history streamline plots for oscillatory lid-driven cavity flow for $Re = 400$ at time $t = 8\mathcal{T} + \beta$; (a) $\beta = 2$, (b) $\beta = 4$, (c) $\beta = 6$, (d) $\beta = 10$, (e) $\beta = 2$, (f) $\beta = 10$.

(i.e., we assumed a priori that a steady-state solution existed) and our numerical results were compared and found to be in excellent agreement with the benchmark numerical solution of Gartling [22], who also used the stationary form of the incompressible Navier–Stokes equations directly.

Here we allow for a transient simulation and are concerned with the fundamental question of whether a steady-state solution exists for the two-dimensional flow over a backward facing step at $Re = 800$. In the study of Gresho et al. [23] this fundamental issue was addressed, in the form of a detailed grid refinement study using four different numerical methods. The study conclusively showed that the two-dimensional flow

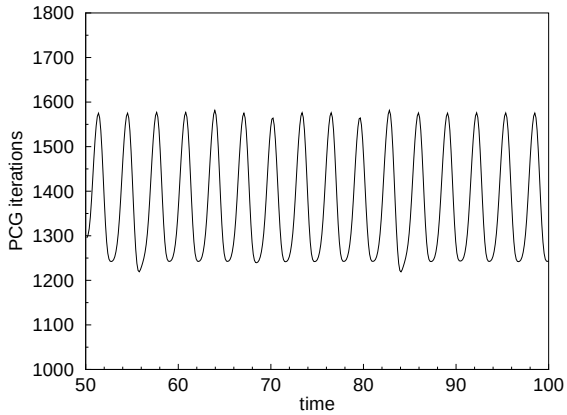

Fig. 13. Time history of PCG iterations for oscillatory lid-driven cavity flow at periodic steady-state flow conditions ($Re = 400$). Jacobi preconditioner with stopping criteria $\varepsilon_{\mathrm{PCG}} = 10^{-6}$.

over a backward-facing step at $Re = 800$ attains a stable (i.e., non-periodic) steady-state. These observations were subsequently confirmed in a study by Fortin et al. [24], using dynamical systems theory, showing that the first Hopf bifurcation point (transition point) for two-dimensional flow over a backward-facing step occurs at least up to $Re = 1600$.

The numerical simulations of Gresho et al. [23] were performed on the simplified step geometry shown in Fig. 14 and among the four numerical methods considered, a (space–time decoupled) spectral element formulation was used. The study of Gresho et al. [23] revealed that inadequate spatial resolution induces chaotic-like temporal behavior, whereas when sufficiently high spatial resolution is used the flow evolves towards a steady-state by a monotonic decay of the transient. This behavior was also observed in the work of Torczynski [25], who performed simulations using the standard step geometry (where the channel portion upstream of the step is included) and also used a (space–time decoupled) spectral element formulation. Adding to the study of Torczynski [25], Yee et al. [26] showed that the initial condition (in addition to the spatial resolution) also strongly influences the temporal behavior of the flow. The spectral element formulations used in these studies resemble that developed by Patera [27], who also performed simulations using the standard step geometry up to $Re = 250$.

In the present study, we wish to investigate the temporal behavior of the two-dimensional flow over a backward-facing step at $Re = 800$ using the proposed least-squares finite element formulation. We consider space–time decoupled and space–time coupled formulations. For comparison of the two formulations, we choose a second-order accurate in time discretization for the temporal terms in constructing the space–time decoupled formulation and restrict the space–time coupled formulation to a p-level of order 2 in time domain.

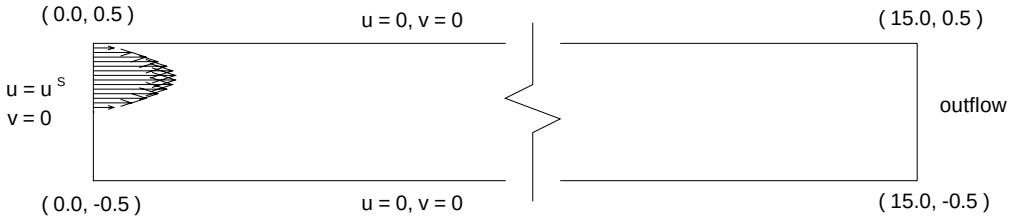

Fig. 14. Geometry and boundary conditions for flow over a backward-facing step: simplified step geometry.

4.4.1. Simplified step geometry

First, the simulations are performed using the simplified step geometry shown in Fig. 14, with the length of the channel extending a distance $L/H = 15$ downstream of the step, which is sufficiently long to preclude undue influence of the finite channel length at this Reynolds number [22,23]. Even though the geometric singularity due to the corner step is excluded by ignoring the portion of the channel upstream of the step, the singularities in pressure and vorticity still exist due to the inlet boundary condition. The Reynolds number is based on the mean inlet velocity and the height of the channel.

The boundary and initial conditions used here are those used in the work of Gresho et al. [23] for the spectral element numerical simulation: $u = v = 0$ on the horizontal walls, $-p + \mu \partial u/\partial n = 0$ and $\partial v/\partial n = 0$ on the outflow boundary, and $u = [\tanh(t/4)]u_B(y) + [1 - \tanh(t/4)]u_P(y)$ and $v = 0$ on the inflow boundary and the step face. Here $u_B(y) = \max[0, 24y(0.5 - y)]$ is the true inlet boundary condition and $u_P(y) = 3(0.5 - y)(0.5 + y)$ is the Poiseuille flow observed infinitely far downstream at steady flow conditions. The initial velocity field is set to $u = u_P(y)$ and $v = 0$ everywhere in the computational domain. Note that the inlet condition is varied fast but smoothly from Poiseuille flow to flow over a backward-facing step, thus inducing a transient wave strong enough to excite sustained unsteady behavior, if that is the correct asymptotic steady-state behavior.

The transient wave will travel through the entire channel length. The main flow coming from the inlet will follow a sinuous path through the channel, forming a series of eddies along the upper and lower wall (see Fig. 18). As the flow evolves, the strength of the eddies should diminish and the two major separation zones near the inlet of the channel attain their steady-state position. Eventually the weaker eddies along the channel length die out and the flow reaches a steady-state. Based on the observations made in the previous work of Gresho et al. [23] and Torczynski [25], high enough spatial resolution should be used to adequately resolve all spatial features of the flow. Otherwise, lack of spatial resolution will induce unrealistic temporal chaotic behavior resulting in an erroneous prediction of the long-term behavior of the flow. The rich physics of the flow and the danger of polluting the long-term behavior of the flow by inadequate spatial resolution render this benchmark problem a challenging one for high-order methods. In addition, as we subsequently show through numerical results, the problem is ideally suited to test and compare the performance of space–time coupled and decoupled formulations.

We discretize the domain, $\bar{\Omega} = [0, 15] \times [-0.5, 0.5]$, using 120 finite elements: four uniformly spaced elements along the height of the channel and 30 uniformly spaced elements along the length of the channel. This mesh coincides with the high resolution mesh in the work of Gresho et al. [23] (although their computational domain extended a distance $L/H = 17$ downstream of the step). The numerical simulation is performed using the unsteady, two-dimensional incompressible Navier–Stokes equations in the vorticity based first-order form. The outflow boundary conditions are imposed in a weak sense through the least-squares functional.

First we use a spatial resolution of order 7, for which Gresho et al. [23] reported a steady monotonic decay of the transient. Recall that, for this simulation, a temporal resolution of order 2 is used for the space–time coupled formulation and a second-order accurate representation (the trapezoidal rule) is used for the temporal terms in the space–time decoupled formulation. A single element layer in time domain is used for the space–time coupled formulation. For the time marching procedure the size of the time step, $\Delta t = t_{s+1} - t_s$, was chosen as $\Delta t = 0.20$ for the space–time coupled and decoupled formulations. We march in time until a steady-state is well established.

The resulting discrete models have a total of 73,428 dof for the space–time coupled finite element model and 24,476 dof for the space–time decoupled finite element model. At each Newton step, the linear system of equations with a SPD coefficient matrix are solved using the conjugate gradient method with a Jacobi preconditioner in matrix-free form. Convergence of the conjugate gradient method was declared when the norm of the residual was less than 10^{-6}. Nonlinear convergence was declared when the relative norm of the

residual in velocities, $\|\Delta \mathbf{u}^{hp}\|/\|\mathbf{u}^{hp}\|$, was less than 10^{-4}, which typically required three Newton iterations per space–time strip/time step.

Fig. 15 shows a plot of the L_2 least-squares functional as a function of time, for the space–time coupled and decoupled formulations. The legend in Fig. 15 describes the resolution of the simulation in space–time and the size of the time step. For example, 7/7/2 $\Delta t = 0.20$ denotes a space–time coupled simulation with isotropic resolution of order 7 in space ($p_\xi = p_\eta = 7$) and order 2 in time ($p_\gamma = 2$), with the size of the time step fixed at 0.20. On the other hand, 7/7/TR $\Delta t = 0.20$ denotes a space–time decoupled simulation with isotropic resolution of order 7 in space and a trapezoidal rule (TR) representation for the temporal terms, with the size of the time step fixed at 0.20.

From Fig. 15 it is clear that the space–time decoupled formulation (for $\Delta t = 0.20$) becomes unstable, forcing an early termination of the simulation. On the other hand, the space–time coupled formulation remains stable throughout; at a lower value of the L_2 least-squares functional than that initially attained by the decoupled formulation. The decoupled formulation is stable at early times, during the smooth transition from Poiseuille flow to flow over a backward-facing step. However, by the time the transient wave reaches the outflow boundary a severe instability had occurred and grown to such extent which forced the termination of the simulation.

Next, we investigate the effect of the time step size on the stability of the decoupled formulation. The results, also plotted in Fig. 15, show that the space–time decoupled formulation remains unstable, even for $\Delta t = 0.05$. In fact, when Δt is decreased the instability starts at earlier times in the simulation – perhaps suggesting a lack of numerical damping (inherent to the TR representation). With this in mind and in an attempt to stabilize the space–time decoupled simulation we implement the generalized α-method (GAM) family of approximations [28–30], which retain second-order accuracy in time and allow for user controlled high frequency damping by the single free integration parameter, $0.0 \leqslant \rho_\infty^h \leqslant 1.0$. For $\rho_\infty^h = 1.0$ the method is identical to the trapezoidal rule and for choices of $0 \leqslant \rho_\infty^h < 1.0$ numerical damping is added with decreasing ρ_∞^h. Fig. 16 shows the time history of the L_2 least-squares functional for the space–time decoupled formulation using the GAM for $\Delta t = 0.10$ and popular choices of ρ_∞^h (see [30]). Increasing the numerical dissipation clearly does not stabilize the simulation.

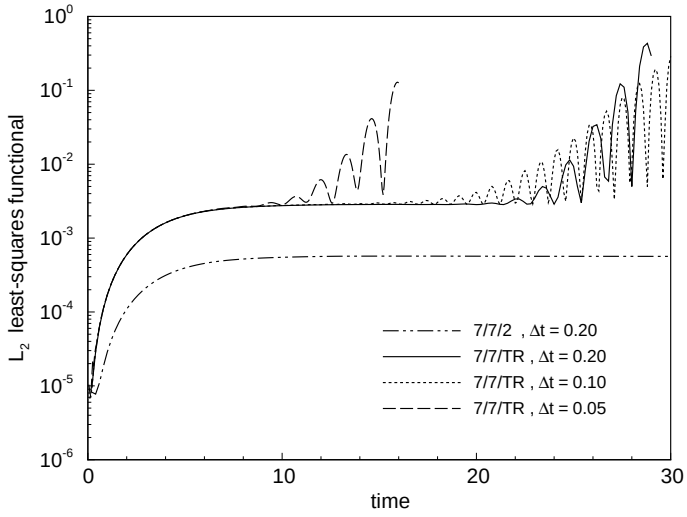

Fig. 15. Time history of the L_2 least-squares functional for space–time coupled and decoupled formulations. Fixed spatial resolution of order 7.

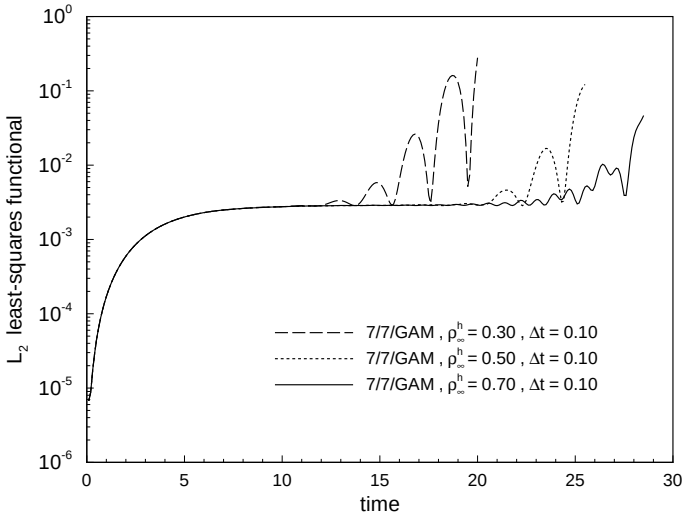

Fig. 16. Time history of the L_2 least-squares functional for space–time decoupled formulation using the GAM. Fixed spatial resolution of order 7.

Realizing the underlying assumption in the decoupled formulation, namely that space and time are decoupled, we are led to believe that the spatial resolution is still not high enough and is inducing chaotic temporal instabilities that cause the space–time decoupled formulation to become unstable. Clearly this observation does not apply to the space–time coupled formulation, where no instability is observed.

Based on the above observation, we increase the spatial resolution of the space–time decoupled simulation to order 9 (having a total of 40,108 dof). For this spatial resolution the space–time decoupled formulation, with TR and $\Delta t = 0.20$, is stable. Fig. 17 shows the time history of the L_2 least-squares functional for the space–time coupled simulation 7/7/2 $\Delta t = 0.20$ and the space–time decoupled formulation 9/9/TR

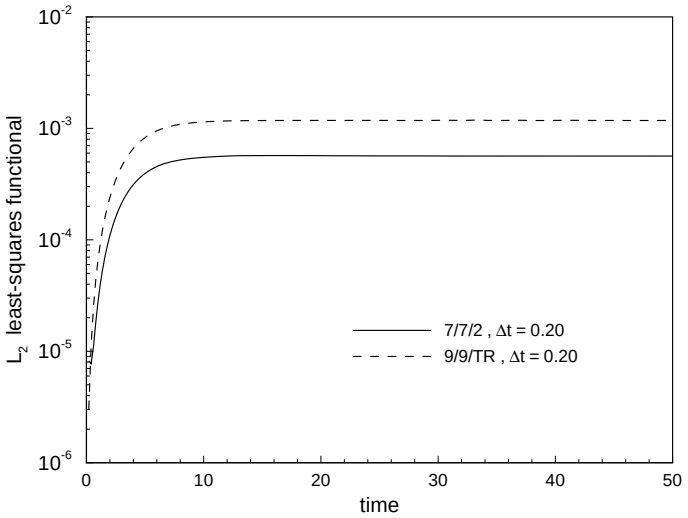

Fig. 17. Time history of the L_2 least-squares functional for space–time coupled simulation 7/7/2 $\Delta t = 0.20$ and decoupled simulation 9/9/TR $\Delta t = 0.20$.

tho ı the space–time deco ıs a higher spatial resolution.
ıtioı with a lower spati ves a lower value for the

ıe r(ive norm of the tween two consecutive sr
r th pace–time coı ıı(ss than 10^{-4} between ı
e–ti decoupled f ıdi(t a steady-state was a
the w field in strea ts, computed using
2 Δt).20). Fi(ıne tim of the v-velocity co
l's m section ce–time /7/2 $\Delta t = 0.20$) a
)). It ieen ı ımulations nibit a monotor
ory d y c ıient, indica ldditional spati
ime ı ɔ' ılation exhibi cillatory tem
thele ı ed steady-state ion is achi
stea(y-s ɔlution reported
is the con ıational cost assoc ch of the
ter? ons ɔr the space–time c($\Delta t = 0.$
d poiıt in the plot is the s eratio
/ ee Newton steps), ing
s(ıat initially both si ire
ıon- ır and PCG con a
g ı ɔ iterations. How

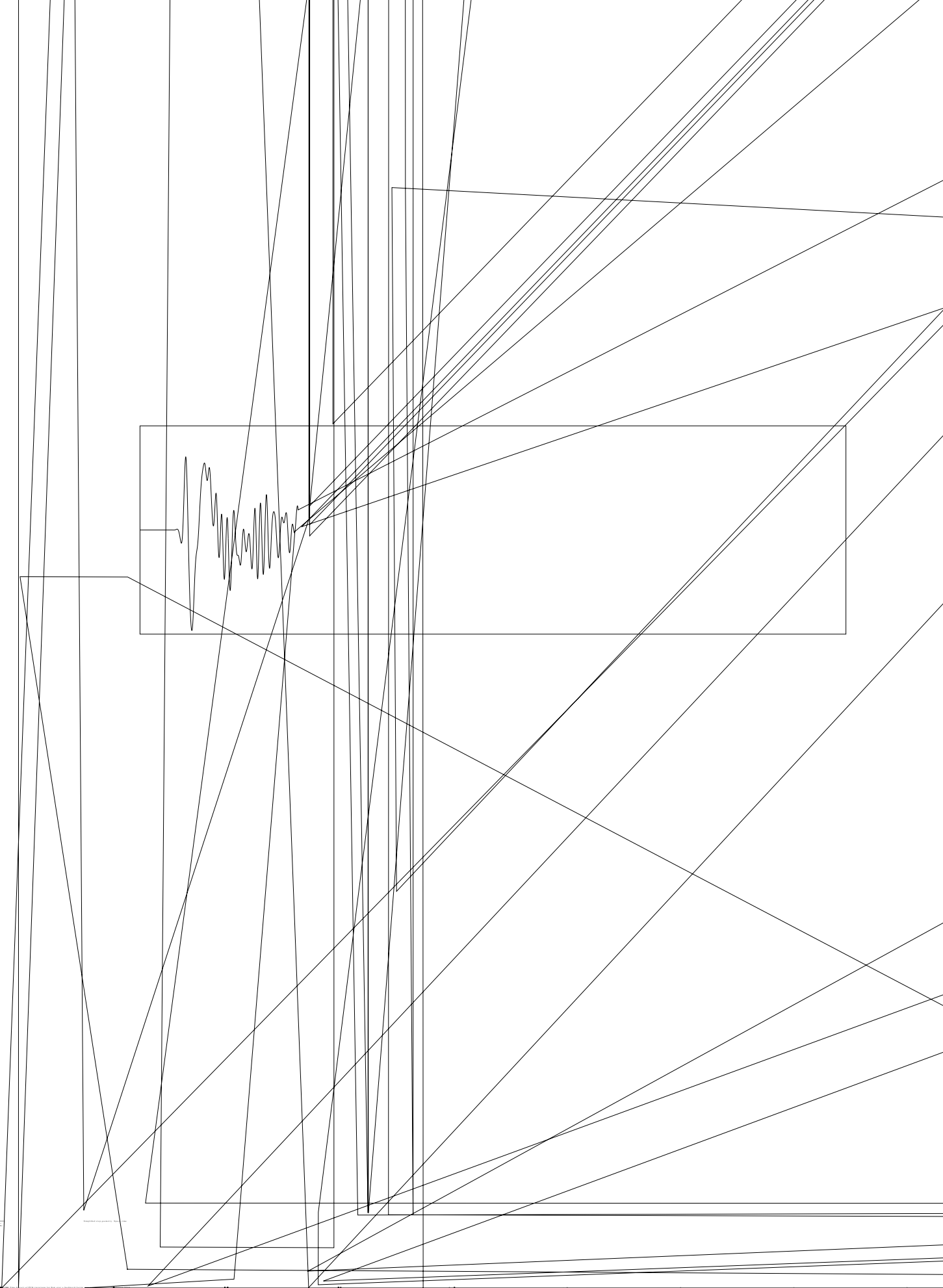

per PCG iteration, having only 40,108 dof, thus resulting in a lower total CPU solve time when compared to the space–time coupled simulation.

In a deliberate attempt to obtain an unstable simulation with the space–time coupled formulation, we decrease the spatial resolution to order 5, and run the simulation 5/5/2 $\Delta t = 0.20$. For such spatial resolution Gresho et al. [23] reported 'numerical errors', denoting termination of the numerical solution due to un-physically large values in velocities. In contrast to the results reported using the (space–time decoupled) spectral element formulation in Gresho et al. [23], the least-squares space–time coupled simulation remained stable and predicted a steady-state. The time history of the v-velocity component at two locations along the channel's mid-section for the simulation 5/5/2 $\Delta t = 0.20$ is shown in Fig. 21. As expected, the decay of the transient displays a more pronounced oscillatory behavior than that obtained for the simulation 7/7/2 $\Delta t = 0.20$, shown in Fig. 19. Nevertheless, the desired stead-state is attained.

4.4.2. Standard step geometry

We now consider the standard step geometry, where a portion of the channel upstream of the step is included. The interest in this configuration is to determine whether the geometric singularity due to the sharp corner step will affect the predictive capabilities of the formulation. It is well-known that high-order methods are very sensitive to geometric singularities and may have difficulty preserving monotonicity in their presence. In this context, high-order methods are not as robust as low-order methods.

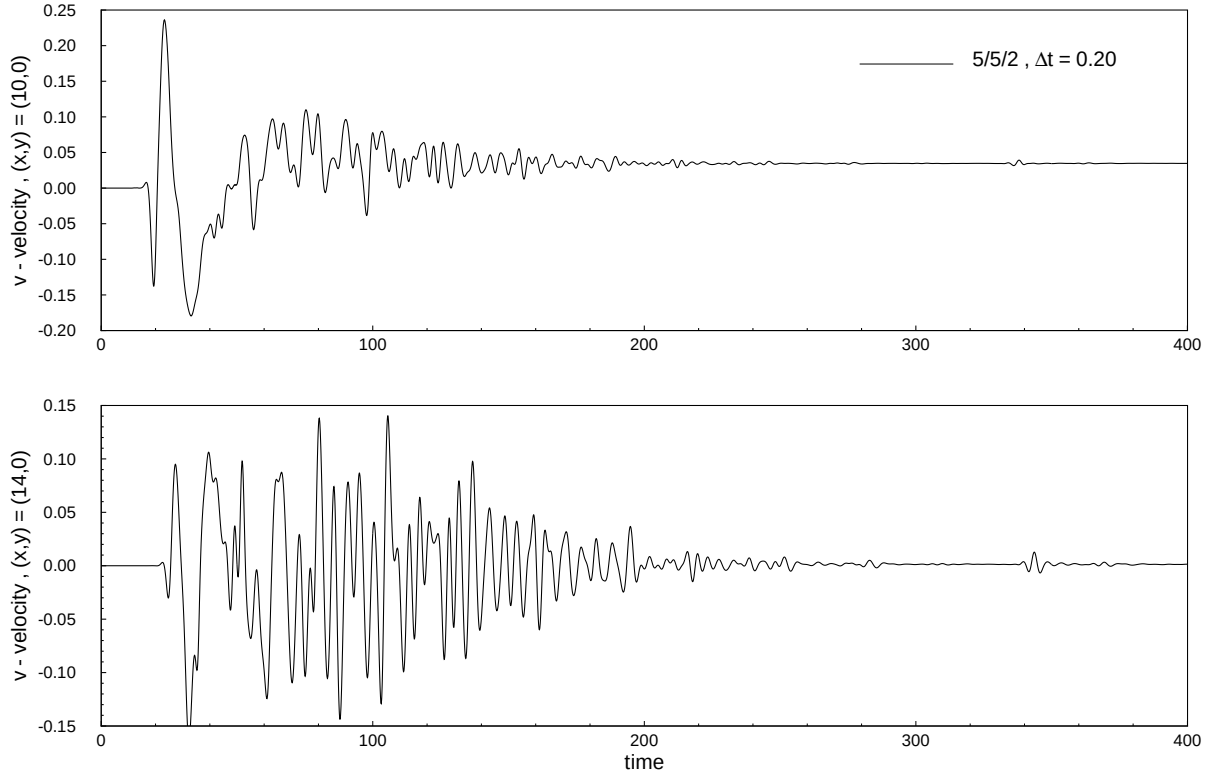

Fig. 21. Time history of the v-velocity component at two selected locations near the exit of the channel: $(x, y) = (10, 0)$ and $(x, y) = (14, 0)$. Space–time coupled simulation 5/5/2 $\Delta t = 0.20$. Simplified step geometry.

plified step geometry, shown in Fig. 14, by
he connected model is the same used for the
refinements near the sharp corner, to the up-
the same as before, with the exception that the
nnel upstream of the step and is of the form:
on the inflow boundary and step surface. The
ed in the work of Torczynski [25] and Yee et al.
geometry and a (space–time decoupled) spectral
of boundary and initial conditions allow flow
hieve a smooth transition from Poiseuille flow to
escribed to take place over a longer period of time,
geometry. More pronounced transitions were not
symptotic behavior of the flow is reported in the

series of streamline plots, computed using the space–
22 it is evident that the sharp corner step did not have
avior) on the flow field.
velocities between two consecutive space–time strips
was achieved. Fig. 23 shows the time history of the v-
for the previously presented simplified step geometry
spatial resolution, the decay of the transient initially

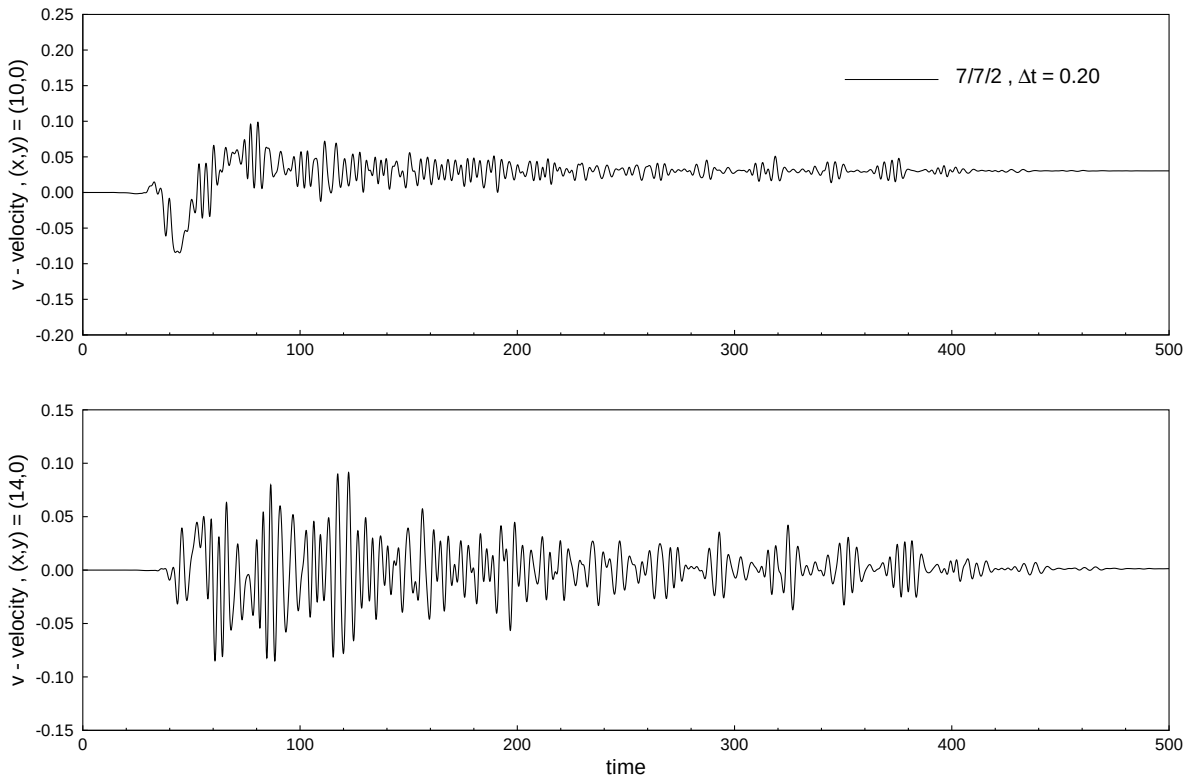

Fig. 23. Time history of the v-velocity component at two selected locations near the exit of the channel: $(x, y) = (10, 0)$ and $(x, y) = (14, 0)$. Space–time coupled simulation 7/7/2 $\Delta t = 0.20$. Standard step geometry.

displays a chaotic-like behavior, then seems to attain a periodic steady-state, and eventually achieves the desired steady-state. The L_2 least-squares functional remained below 10^{-3} throughout the simulation. The PCG iteration history for the simulation is shown in Fig. 24 and is not much different from the one obtained for the simplified step geometry simulation, indicating that the sharp corner step did not have marked effects on the conditioning of the coefficient matrix. The space–time decoupled simulations with spatial resolution of order 7 and 9 and time step size $\Delta t = 0.20$, became unstable resulting in early termination.

The above results (for the simplified and standard step geometry) indicate that the least-squares space–time coupled formulation for unsteady two-dimensional simulations is robust, computationally-cost competitive, and has superior predictive capabilities when compared to the space–time decoupled formulation. This problem is clearly more demanding, in terms of space–time resolution, than the previously considered unsteady cavity flows. For the lid-driven cavity flows considered earlier, the space–time coupled and decoupled formulations give indistinguishable time histories. However, in general, we can never classify a problem a priori as needing low or high space–time resolution. In this sense, space–time coupled formulations represent an attractive and affordable alternative to space–time decoupled formulations.

For problems where the singularities due to sharp corners may be more severe (e.g., 2-D flow past a square cylinder), the use of conforming discretizations using high-order element expansions is generally not appropriate or efficient. Such problems may be better handled with a collocation least-squares approach, using a bi-linear basis.

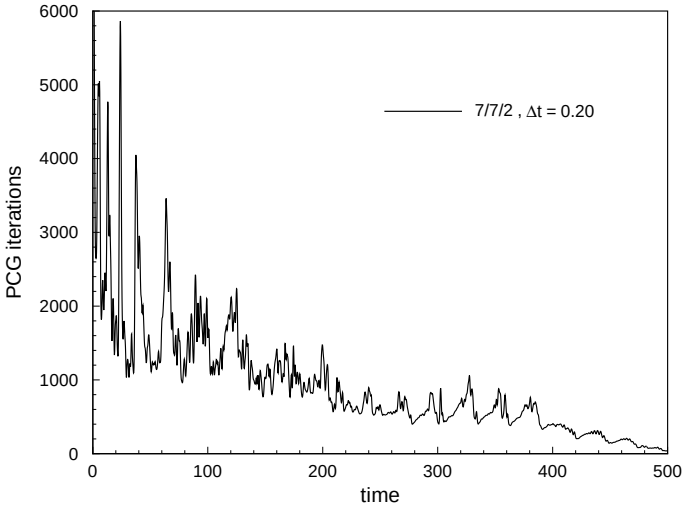

Fig. 24. Time history of PCG iterations for flow over a backward-facing step ($Re = 800$). Standard step geometry. Space–time coupled simulation 7/7/2 $\Delta t = 0.20$. Jacobi preconditioner with stopping criteria $\varepsilon_{\mathrm{PCG}} = 10^{-6}$.

4.5. Flow past a circular cylinder

We consider the two-dimensional flow of an incompressible fluid past a circular cylinder. At low Reynolds numbers ($5 < Re < 40$) the flow is stationary and characterized by a pair of standing vortices appearing behind the cylinder. The size of the separated flow region increases with increasing Reynolds number, until a limit in which the wake becomes unstable. At this critical Reynolds number, $Re_{\mathrm{c}} \approx 46.2$ [31,32], vortices are shed from the aft of the circular cylinder, forming the well-known von Karman vortex street. The flow may be treated as two-dimensional until $Re_{\mathrm{c}}^{\text{3-D}} \approx 188.5$ [33], at which point the cylinder wake becomes three-dimensional due to a secondary instability of the vortex street.

From the numerical simulation point of view, the interest of this problem is in the accurate resolution of the vortex street and the modelling of the outflow boundary conditions, the latter which arises from the necessity of truncating the domain in a region where the vortex street is fully developed. This transient problem is frequently used to assess the accuracy of time-marching numerical procedures and open boundary conditions, as it is characterized by several important flow parameters, such as the non-dimensional frequency of the vortex shedding (the Strouhal number), the amplitude of the lift coefficient, and the mean drag coefficient.

The cylinder is of unit diameter and is placed in the finite region $\bar{\Omega} = [-15.5, 25.5] \times [-20.5, 20.5]$. The center of the cylinder lies at $(x, y) = (0, 0)$, so that the inflow boundary is located 15.5 cylinder diameters in front of the center of the cylinder and the outflow boundary 25.5 cylinder diameters downstream of the center of the cylinder. The top and bottom boundaries are located each 20.5 cylinder diameters above and below the center of the cylinder. The Reynolds number is based on the free-stream velocity and cylinder diameter.

Having considered a large computational domain allows us to impose free-stream boundary conditions at the top and bottom of the domain without noticeably affecting the solution. The boundary conditions include a specified value of 1.0 for the x-component of velocity at the inflow, top, and bottom boundaries, i.e., the free-stream velocity u_∞ is specified to be unity. At these boundaries the y-component of velocity is

dary conditions are specified at the cylinder surface: $u = v = 0$. The outflo
(30), are imposed in a weak sense through the least-squares functional:

$$\frac{\partial \mathbf{u}}{\partial t} + (\mathbf{u}\cdot\nabla)\mathbf{u} + \nabla p + \frac{1}{Re}\nabla\times\boldsymbol{\omega} - \mathbf{f}\Big\|^2_{0,\Omega\times(0,\tau]} + \|\boldsymbol{\omega} - \nabla\times\mathbf{u}\|^2_{0,\Omega\times(0,\tau]}$$

$$\cdot\,\mathbf{u}\|^2_{0,\Omega\times(0,\tau]} + \|\nabla\cdot\boldsymbol{\omega}\|^2_{0,\Omega\times(0,\tau]} + \|\hat{\mathbf{n}}\cdot\tilde{\boldsymbol{\sigma}}\|^2_{0,\Gamma_{\text{outflow}}\times(0,\tau]}\Bigg).$$

t and the free-stream velocity is gradually increased in time from 0.0 to 1.0 ac
igent distribution, $u_\infty(t) = \tanh(t)$. An alternate initial condition is a steady-stat
he steady-state solver). The final periodic steady-state should be independent o
ition.

space–time, $\bar{\Omega}^h = \bar{\Omega}^h \times [t_s, t_{s+1}]$, consists of 501 finite elements in space and a
. Fig. 25(a)–(c) shows the connected model and a close-up view of the geometric
circular cylinder. In the previous examples a subparametric formulation using a
ng, $\bar{\Omega}_e \rightleftarrows \hat{\Omega}_e$, was sufficient to exactly represent the straight-sided geometries. In
nt the circular surface, we implement an isoparametric formulation; i.e., we use
for the element degrees of freedom and for the mapping, $\bar{\Omega}_e \rightleftarrows \hat{\Omega}_e$.

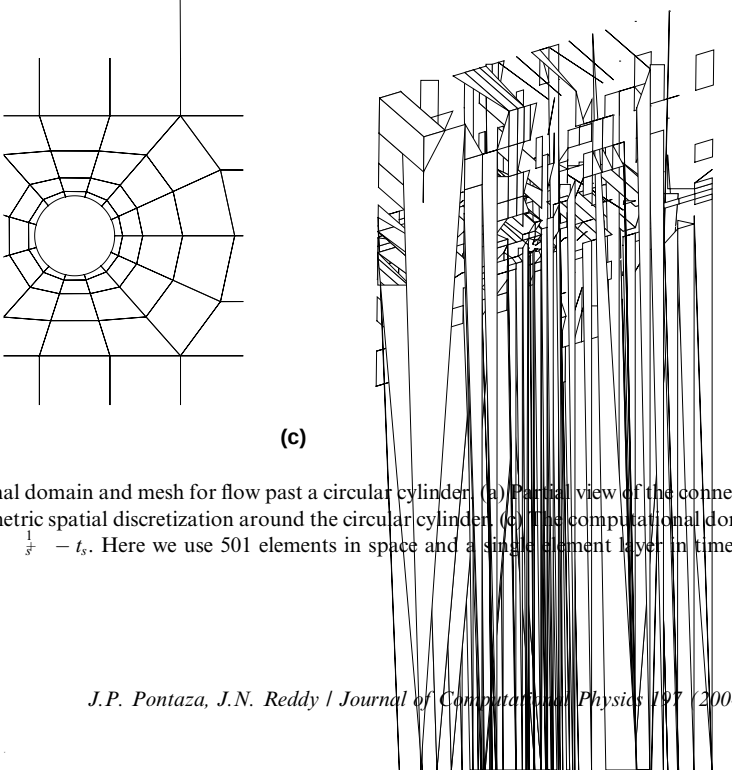

Fig. 25. Space–time computational domain and mesh for flow past a circular cylinder. (a) Partial view of the connected model in space, $\bar{\Omega}^h$. (b) Close-up view of the geometric spatial discretization around the circular cylinder. (c) The computational domain is a space–time strip, denoted by $\bar{\Omega}$, with $t_{s+1} - t_s$. Here we use 501 elements in space and a single element layer in time.

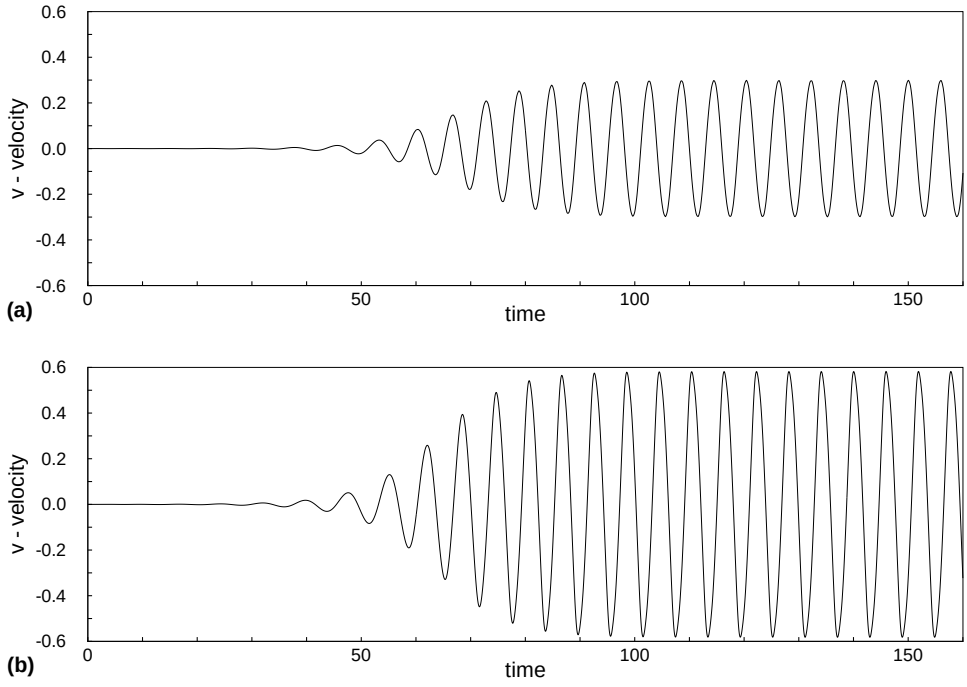

Fig. 26. Time history of v-velocity component behind the circular cylinder: (a) $(x, y) = (1, 0)$ and (b) $(x, y) = (2, 0)$.

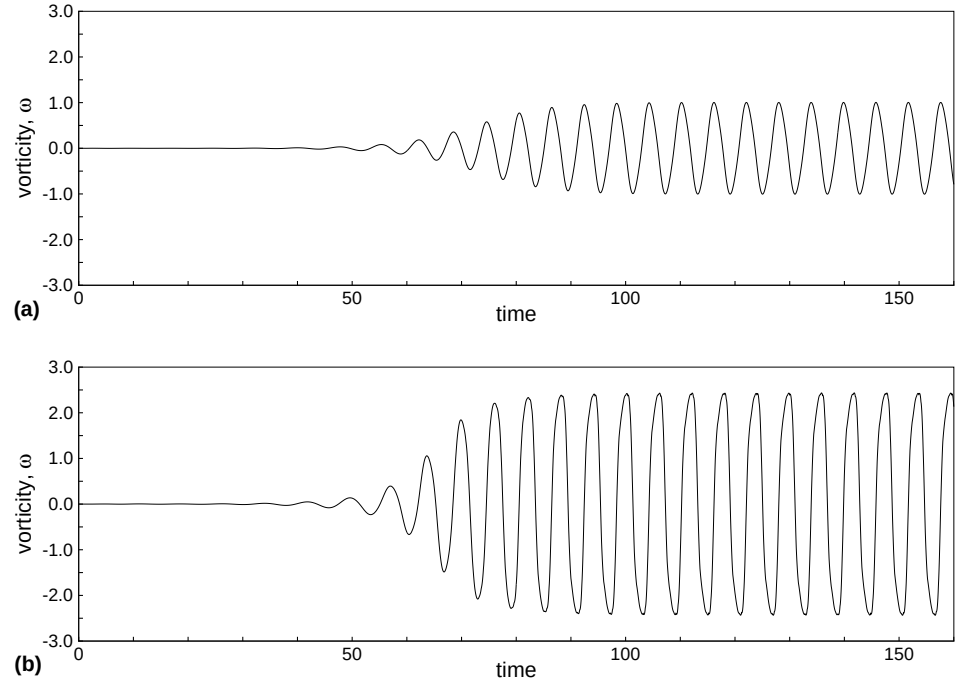

Fig. 27. Time history of vorticity behind the circular cylinder: (a) $(x, y) = (1, 0)$ and (b) $(x, y) = (2, 0)$.

The Reynolds number considered here is 100. We use nodal expansions with $p_\xi = p_\eta = 4$ and $p_\gamma = 3$ in each element. At each Newton step the linear system of algebraic equations is solved using the matrix-free conjugate gradient algorithm with a Jacobi preconditioner. For the time marching procedure the size of the time step, $\Delta t = t_{s+1} - t_s$, was chosen as $\Delta t = 0.50$.

We march in time until a periodic steady-state is well established. Convergence of the conjugate gradient method was declared when the norm of the residual was less than 10^{-6}. Nonlinear convergence was declared when the relative norm of the residual in velocities between two consecutive iterations was less than 10^{-4}, which typically required three Newton iterations per space–time strip. The L_2 space–time least-squares functional remained below 10^{-3} throughout the time marching procedure.

We choose two points in the near wake of the cylinder to trace the change of the velocity components and vorticity with time. Figs. 26 and 27 show the time history of the v-velocity component and vorticity at the points $(x, y) = (1, 0)$ and $(x, y) = (2, 0)$, located 0.5 and 1.5 cylinder diameters behind the cylinder. From the figures we see that shedding starts around $t = 50$. No artificial perturbation is used to induce the vortex shedding. The flow reaches a periodic steady-state by $t = 100$. The period for the v-velocity component is the same as that for the vorticity. The shedding period, obtained from Fig. 26 to within 0.05 time units, is found to be $\mathscr{T} = 6.05$; which gives a dimensionless shedding frequency of $St = 0.1653$. Our results are in good agreement with the experimental measurements of Williamson [34] and with the high-order splitting spectral/*hp* numerical results of Sherwin and Karniadakis [35], reported as $St = 0.1643$ and 0.1667, respectively.

The viscous and pressure forces acting on the cylinder are given by

$$\mathbf{F}_s = \oint \mu \left[(\nabla \mathbf{u}) + (\nabla \mathbf{u})^{\mathrm{T}} \right] \cdot \hat{\mathbf{n}} \, \mathrm{d}s, \quad \mathbf{F}_p = - \oint p \hat{\mathbf{n}} \, \mathrm{d}s$$

and the corresponding force coefficients obtained by normalizing the forces by the dynamic pressure, $\frac{1}{2}\rho u_\infty^2$, acting on a unit span of the circular cylinder. The predicted average drag coefficient is $\bar{C}_{\mathrm{D}} = 1.345$, in good agreement with the high-order splitting spectral/*hp* numerical results of Henderson [33], reported as $\bar{C}_{\mathrm{D}} = 1.35$. The amplitude of the lift coefficient is predicted as $C_{\mathrm{L}} = \pm 0.332$. Fig. 28 shows the time history of the lift coefficient with its pressure and viscous contributions.

Fig. 29 depicts the vortex shedding cycle behind the circular cylinder by showing vorticity contours at four successive times during one period. Eddies are formed behind the cylinder and are washed away into

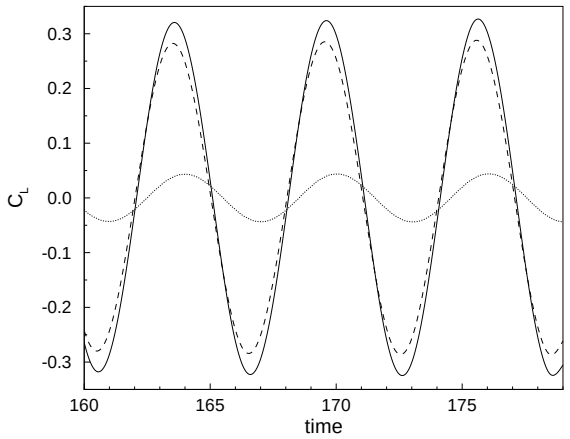

Fig. 28. Time history of lift coefficient (solid line). Shown is also the pressure contribution (dashed line) and the viscous contribution (dotted line).

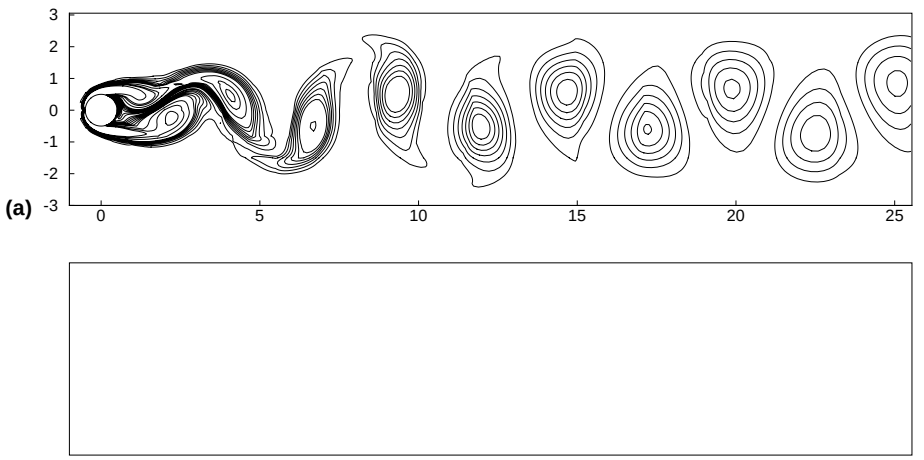

the wake region. This flow pattern is popularly known as the von Karman vortex street. Two eddies, alternatively of positive and negative vorticity, are shed within each period from the aft of the circular cylinder. Fig. 30 shows instantaneous velocity and pressure contours at the reference dimensionless time $t_0 = 160$. From visual inspection of the contour plots in Figs. 29 and 30 it is clear that the outflow boundary condition allows the flow to exit the computational domain gracefully and does not disturb the upstream flow.

Even though results were presented for the simulation 4/4/3 $\Delta t = 0.50$, we also performed simulations with lower time domain resolution, lower Δt, higher h-resolution, and with space–time decoupled formulations. We present results for these simulations in the form of computational cost metrics, essential in evaluating the overall performance of the formulation.

Fig. 31 shows the time histories of PCG iterations for space–time coupled simulations 4/4/3 $\Delta t = 0.50$ in two different meshes. Mesh A consists of 501 finite elements in space and a single element layer in time and is shown in Fig. 25. Mesh B is an h-refined version of mesh A, with 792 finite elements in space and a single

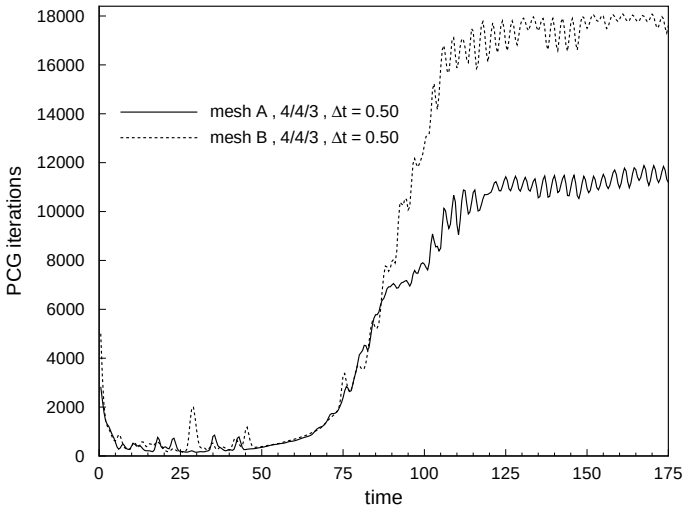

Fig. 31. Time history of PCG iterations for space–time coupled simulations 4/4/3 $\Delta t = 0.50$ in meshes A and B. Jacobi preconditioner with stopping criteria $\varepsilon_{\mathrm{PCG}} = 10^{-6}$.

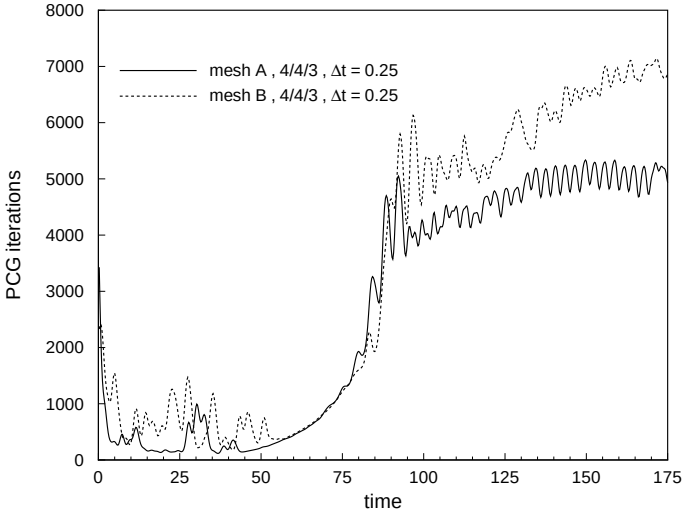

Fig. 32. Time history of PCG iterations for space–time coupled simulations 4/4/3 $\Delta t = 0.25$ in meshes A and B. Jacobi preconditioner with stopping criteria $\varepsilon_{\mathrm{PCG}} = 10^{-6}$.

convergence. However, the simulations (up to $t = 175$) required the sequential solution of 700 space–time strips, resulting in only slightly lower total CPU solve times when compared to the cases 4/4/3 $\Delta t = 0.50$. The computed characteristic flow parameters for these simulations presented negligible differences (as much as 0.01%) with those reported previously for the case 4/4/3 $\Delta t = 0.50$ using mesh A.

Fig. 33 shows the time histories of PCG iterations for space–time coupled simulation 4/4/2 $\Delta t = 0.10$ and space–time decoupled simulations 4/4/GAM $\rho_\infty^h = 0.50$ and 4/4/TR (equivalent to 4/4/GAM $\rho_\infty^h = 1.0$) with $\Delta t = 0.10$ using mesh A. The simulations (up to $t = 175$) require the sequential solution of 1750 space–time strips/time steps. From Fig. 33 we see that the space–time coupled formulation has better matrix

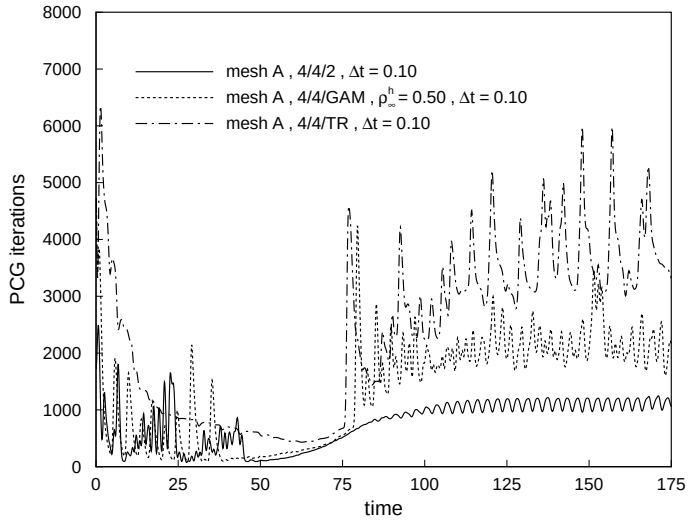

Fig. 33. Time history of PCG iterations for space–time coupled and decoupled simulations with $\Delta t = 0.10$ in mesh A. Jacobi preconditioner with stopping criteria $\varepsilon_{\mathrm{PCG}} = 10^{-6}$.

conditioning than the decoupled formulations, resulting in faster PCG convergence. However, the space–time decoupled simulations require less work per PCG iteration, having only 32,864 dof compared to 98,592 dof for the space–time coupled simulation, thus resulting in approximately equal CPU solve times. To give the reader a feeling of the algorithmic performance achieved by the formulation in actual implementations, we report the solution time of the space–time coupled simulation 4/4/2 $\Delta t = 0.10$ as 4.5 wall-clock hours using 8 processors (R14K at 500 MHz) in a SGI Origin 3800.

The PCG iteration history for the space–time decoupled simulations displays a more pronounced oscillatory behavior than that observed for the space–time coupled simulations. In addition, we observe that

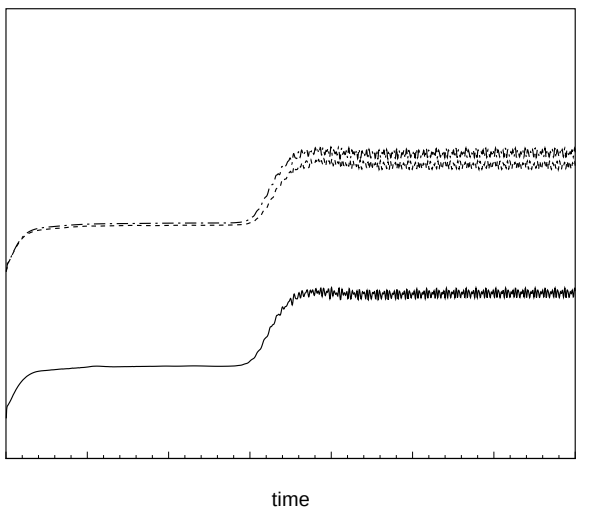

the trapezoidal rule (TR) simulation results in a higher computational cost when compared to the GAM [28–30] simulation with a high frequency damping parameter of $\rho_\infty^h = 0.50$. Fig. 34 shows the time history of the L_2 least-squares functional for these simulations. In the periodic steady-state the value of the L_2 least-squares functional for the space–time coupled formulation is approximately two orders of magnitude lower than that for the decoupled formulation. The cost-accuracy metrics indicate that the space–time coupled formulation is the optimal choice.

Remark. The two-dimensional flow past a circular cylinder can be categorized as an external flow problem, where the cylinder is immersed in an unbounded fluid. Sufficiently far away upstream of the cylinder, the flow field is uniform with $p = p_\infty$. In addition, sufficiently far away downstream of the cylinder the pressure field is essentially uniform (except for small variations in the wake region) with $p = p_\infty$. The simulations were also carried out by specifying the consistent boundary condition $p = p_\infty$ at the inflow region. Without this additional consistent boundary condition, the space–time decoupled simulation became unstable. The space–time coupled simulation did not display such sensitivity to the boundary condition, however specifying the additional consistent boundary condition improved PCG convergence.

5. Concluding remarks

In this paper we presented a space–time coupled least-squares finite element formulation for the non-stationary advection-diffusion and incompressible Navier–Stokes equations. Formulations based on least-squares principles offer many theoretical and computational advantages in the implementation of the corresponding finite element model that are not present in the traditional weak form Galerkin finite element model. Most notably, the use of least-squares principles leads to a variational unconstrained minimization problem where stability conditions such as inf–sup conditions never arise. In addition, the finite element model always yields a discrete system of equations with a SPD coefficient matrix, allowing the use of robust and fast iterative methods for its solution.

High order nodal/modal expansions in both space and time were used to develop the finite element models. A time-stepping procedure in which the solution is obtained for space–time strips in a sequential manner was implemented. In each space–time strip the SPD coefficient matrix is solved in a fully coupled manner (i.e., no splitting) using the conjugate gradient method with a Jacobi preconditioner in matrix-free form.

The merits of the formulation were demonstrated through numerical examples. For the advection-diffusion equation we considered the transport of a scalar field in a rotating flow field, where the pure advection limit was tested. For the incompressible Navier–Stokes equations we presented results for impulsively started lid-driven cavity flow, oscillatory lid-driven cavity flow, transient flow over a backward-facing step, and flow around a circular cylinder. Introducing a basis in time domain allowed us to represent the time evolution of the flow fields with arbitrary accuracy by *hp* refinements, hence stability of the time-stepping procedure was not an issue and relatively large time steps were used in the numerical examples to illustrate this property. The quality of the numerical solution was judged by the value of the L_2 least-squares functional, which was shown to decay exponentially fast as the expansion order of the element basis is increased. The space–time coupled formulation showed superior predictive capabilities for flows demanding high space–time resolution, exemplified here by the transient flow over a backward-facing step, and was found to be computationally-cost competitive compared to space–time decoupled formulations for two-dimensional unsteady problems. For three-dimensional unsteady problems (not considered in the present study), a space–time coupled approach is currently prohibitively expensive and a decoupled approach must be used.

Acknowledgements

The support of this research by the Computational Mathematics Program of the Air Force Office of Scientific Research (F49620-03-1-0201) is gratefully acknowledged. The first author also acknowledges the support of this work through a Computational Science and Engineering Program Graduate Fellowship from Texas A&M University.

References

[1] J.P. Pontaza, J.N. Reddy, Spectral/*hp* least-squares finite element formulation for the Navier–Stokes equations, J. Comput. Phys. 190 (2003) 523.
[2] J.N. Reddy, An Introduction to the Finite Element Method, second ed., McGraw-Hill, New York, 1993.
[3] J.N. Reddy, An Introduction to Nonlinear Finite Element Analysis, Oxford University Press, 2004.
[4] B.N. Jiang, The Least-Squares Finite Element Method, Springer, Berlin, 1998.
[5] L.Q. Tang, T.H. Tsang, A least-squares finite element method for time-dependent incompressible flows with thermal convection, Int. J. Numer. Meth. Fluids 17 (1993) 271.
[6] P.B. Bochev, Analysis of least-squares finite element methods for the Navier–Stokes equations, SIAM J. Numer. Anal. 34 (1997) 1817.
[7] P.B. Bochev, M.D. Gunzburger, Finite element methods of least-squares type, SIAM Rev. 40 (1998) 789.
[8] Z. Cai, T.A. Manteuffel, S.F. McCormick, First-order system least-squares for the Stokes equations, with applications to linear elasticity, SIAM J. Numer. Anal. 34 (1997) 1727.
[9] M.M.J. Proot, M.I. Gerrtisma, Least-squares spectral elements applied to the Stokes problem, J. Comput. Phys. 181 (2002) 454.
[10] B.C. Bell, K.S. Surana, A space–time coupled *p*-version least-squares finite element formulation for unsteady fluid dynamics problems, Int. J. Numer. Meth. Engng. 37 (1994) 3545.
[11] B.C. Bell, K.S. Surana, A space–time coupled *p*-version least-squares finite element formulation for unsteady two-dimensional Navier–Stokes equations, Int. J. Numer. Meth. Engng. 39 (1996) 2593.
[12] T.C. Warburton, S.J. Sherwin, G.E. Karniadakis, Basis functions for triangular and quadrilateral high-order elements, SIAM J. Sci. Comput. 20 (1999) 1671.
[13] G.E. Karniadakis, S.J. Sherwin, Spectral/*hp* Element Methods for CFD, Oxford University Press, Oxford, 1999.
[14] J.N. Reddy, Energy Principles and Variational Methods in Applied Mechanics, second ed., John Wiley, New York, 2002.
[15] Y. Saad, Iterative Methods for Sparse Linear Systems, PWS Publishing Company, 1996.
[16] G.H. Golub, C.F.V. Loan, Matrix Computations, third ed., John Hopkins University Press, Baltimore, MD, 1996.
[17] R.L. Sani, P.M. Gresho, Resume and remarks on the open boundary condition minisymposium, Int. J. Numer. Meth. Fluids 18 (1994) 983.
[18] D. Winterscheidt, K.S. Surana, *p*-version least-squares finite element formulation for two-dimensional incompressible fluid flow, Int. J. Numer. Meth. Fluids 18 (1994) 43.
[19] U. Ghia, K.N. Ghia, C.T. Shin, High-Re solution for incompressible flow using the Navier–Stokes equations and the multigrid method, J. Comput. Phys. 48 (1982) 387.
[20] R. Iwatsu, J.M. Hyun, K. Kuwahara, Numerical simulation of flows driven by a torsionally oscillating lid in a square cavity, J. Fluids Engng. 114 (1992) 143.
[21] W.Y. Soh, J.W. Goodrich, Unsteady solution of incompressible Navier–Stokes equations, J. Comput. Phys. 79 (1988) 113.
[22] D.K. Gartling, A test problem for outflow boundary conditions – flow over a backward-facing step, Int. J. Numer. Meth. Fluids 11 (1990) 953.
[23] P.M. Gresho, D.K. Gartling, J.R. Torczynski, K.A. Cliffe, K.H. Winters, T.J. Garrat, A. Spence, J.W. Goodrich, Is the steady viscous incompressible two-dimensional flow over a backward-facing step at $Re = 800$ stable?, Int. J. Numer. Meth. Fluids 17 (1993) 501.
[24] A. Fortin, M. Jardak, J.J. Gervais, R. Pierre, Localization of Hopf bifurcations in fluid flow problems, Int. J. Numer. Meth. Fluids 24 (1997) 1185.
[25] J.R. Torczynski, A grid refinement study of two-dimensional transient flow over a backward-facing step using a spectral element method, in: J.C. Dutton, L.P. Purtell (Eds.), Separated Flows, vol. 149, ASME, 1993.
[26] H.C. Yee, J.R. Torczynski, S.A. Morton, M.R. Visbal, P.K. Sweby, On spurious behavior of CFD simulations, Int. J. Numer. Meth. Fluids 30 (1999) 675.
[27] A.T. Patera, A spectral element method for fluid dynamics: laminar flow in a channel expansion, J. Comput. Phys. 54 (1984) 468.

[28] J. Chung, G.M. Hulbert, A time integration algorithm for structural dynamics with improved numerical dissipation: The generalized α-method, J. Appl. Mech. 60 (1993) 371.
[29] K.E. Jansen, C.H. Whitting, G.M. Hulbert, A generalized α-method for integrating the filtered Navier–Stokes equations with a stabilized finite element method, Comput. Methods Appl. Mech. Engrg. 190 (2000) 305.
[30] W. Dettmer, D. Peric, An analysis of the time integrator algorithms for the finite elelemt solutions of incompressible Navier–Stokes equations based on a stabilised formulation, Comput. Methods Appl. Mech. Engrg. 192 (2003) 1177.
[31] C.P. Jackson, A finite-element study of the onset of vortex shedding in flow past variously shaped bodies, J. Fluid Mech. 182 (1987) 23.
[32] J. Dušek, P. Le Gal, P. Fraunié, A numerical and theoretical study of the first Hopf bifurcation in a cylinder wake, J. Fluid Mech. 264 (1994) 59.
[33] R.D. Henderson, Details on the drag curve near the onset of vortex shedding, Phys. Fluids 7 (1995) 2102.
[34] C.H.K. Williamson, Oblique and parallel modes of vortex shedding in the wake of a circular cylinder at low Reynolds numbers, J. Fluid Mech. 206 (1989) 579.
[35] S.J. Sherwin, G.E. Karniadakis, A triangular spectral element method; applications to the incompressible Navier–Stokes equations, Comput. Methods Appl. Mech. Engrg. 123 (1995) 189.